The Institution of Engineering and Technology WILEY

ORIGINAL RESEARCH

Stability improvement of MMC-based hybrid AC/DC grids through the application of a decentralized optimal controller

Atousa Elahidoost[1] | Elisabetta Tedeschi[1,2]

[1]Department of Electric Power Engineering, Norwegian University of Science and Technology, Trondheim, Norway

[2]Department of Industrial Engineering, University of Trento, Trento, Italy

Correspondence
Atousa Elahidoost, Department of Electric Power Engineering, Norwegian University of Science and Technology, 7491 Trondheim, Norway.
Email: atousa.elahidoost@ntnu.no

Funding information
DNV; The Research Council of Norway (Norges Forskningsrådet), Grant/Award Number: IDeCON

Abstract

Interconnection and expansion of AC networks through high-voltage direct current grids based on modular multilevel converters to form a multiterminal hybrid AC/DC grid can pose stability issues. These challenges can arise from dynamic interactions between/within AC and DC subgrids due to poorly damped modes that are potential sources of persistent and disruptive oscillations. This paper aims to ensure the stability of multiterminal hybrid AC/DC grids via a decentralized optimal controller. The proposed methodology analytically and simultaneously identifies both the decentralized optimal controller and the worst-case perturbation scenario under the grid control inputs' and state variables' constraints, without the need for detailed and time-consuming dynamic simulations of all possible scenarios. Eigenvalue stability analysis and time-domain simulations show that the proposed controller can efficiently enhance the test grid stability margins and reduce the oscillations, not only under the worst-case perturbation scenario (increasing damping ratios of the two pairs of least damped modes by 2.34 and 4.05 times) but also under other critical fault conditions. Furthermore, the controller's superior performance is validated through comparison with the power system stabilizer and modular multilevel converter droop controller under small and large disturbances, and its robustness is assessed against parametric uncertainties.

1 | INTRODUCTION

The high-voltage direct current (HVDC) grids based on the modular multilevel converters (MMCs) are playing an increasingly pivotal role in the green shift towards the carbon-free renewable power system [1, 2]. This paradigm is due to the HVDC technology's significant developments in recent years, resulting in higher energy efficiency, power capacity, and controllability of the power system. Hence, the technology has become a viable solution for the interconnection of offshore wind farms and onshore grids to form a multiterminal system topology. In addition, overlay HVDC grids interconnecting synchronous and asynchronous zones over ultra-long distances are essential in achieving a wide-area power system at a (trans-) continental scale, and consequently, the global energy interconnection (GEI) scenario [3].

Notwithstanding the progressive achievements and innovations in HVDC systems, the interconnection of the currently existing and future-built HVDC grids that may have been originally planned and developed without detailed analyses of then-unforeseen grid expansion's effects can eventually induce interoperability issues. These include interactions and stability challenges in multiterminal hybrid AC/DC grids [4–6]. Such dynamic interactions, either on the AC- or DC side of the multiterminal grid, can be a source of detrimental oscillations and propagate to the entire network due to the droop control action of the HVDC converters, resulting in stability deterioration, faults, and subsequent blackouts with considerable damages and costs [7, 8]. Stability problems with oscillations and harmonic interactions have been reported in several HVDC-dominated grids over the past few years, such as harmonic interactions and high-frequency resonances detected at BorWin1 wind farm [9, 10], subsynchronous oscillations observed over a hundred times at Xinjiang wind farm [11], and oscillations reported in several MMC-based HVDC grids in China and Germany [12]. Namely, the oscillations observed worldwide in MMC-based HVDC

systems can occur from the subsynchronous to medium- and high-frequency ranges [12].

A number of recent studies have addressed the control and stability challenges in multiterminal hybrid AC/DC grids [5, 12]. The potential detrimental dynamic interactions between the AC and DC subnetworks are assessed through the impedance-based modelling of the hybrid AC/DC grids in [13]. The AC grid here is represented through a simplified model of the synchronous generator with an automatic voltage regulator (AVR)/exciter, and the considered converter topology is the conventional 2-level voltage source converter (VSC). This study shows that a retuning in the control parameters and a DC-side damper structure are required to assure the grid's stability when the AC and DC grids are interconnected. Reference [14] investigates the effect of the VSC-HVDC links on the transient stability of the AC power systems. A simplified representation of the power system with VSCs modelled as complex current sources with independent active and reactive power injections is used here. A linearizing feedback controller, which requires communications among generators and converter stations, is introduced to improve the stability margins of the AC-side rotor angles by readjusting the active power reference of the power-mode VSCs. In [15], the primary goal is to analyse the modes of interactions and improve the stability margins of the MMC-based HVDC grids. Hence, an adaptive phase locked loop (PLL) controller is proposed to guarantee the grid stability under the short circuit ratio (SCR) and grid inductance variations while requiring communications between all grid components. The MMCs here are modelled as conventional 2-level VSCs by disregarding the converter arm voltages and currents dynamics. Reference [16] proposes a global model predictive control (MPC)-based grid controller to improve the VSC-HVDC grid stability. This controller results in damping the AC network power oscillations by manipulating the HVDC links' power injections. The methodology can react to power system variations without additional tuning; however, it demands communication among HVDC terminals. The VSCs here are also modelled as 2-level converters. A distributed supplementary controller is presented in [17] to enhance rotor angle stability of the VSC-based AC/DC systems. The proposed control law locally computes the control input limits; however, it depends on the communication between converter stations. Moreover, limits on the converters and their controllers are not considered here except those on the converters' power references. Furthermore, AC/DC system modelling contains simplifications on generators, cables, and VSCs, which are represented as converters with controllable active power injections.

In fact, in all the abovementioned references on hybrid AC/DC grid stability analysis, the internal dynamics of the MMCs caused by the circulating currents are ignored, as these currents are not suppressed through either control or modulation. Namely, the critical effect of the MMCs' arm voltages and currents dynamics on the stability of the multiterminal hybrid AC/DC grids and their interactions with the AC-side generators are underestimated. Moreover, none of the references' proposed methodologies to overcome the challenges of the dynamic interactions in hybrid AC/DC grids (except for [16])

is optimal. The solutions do not guarantee stability under the worst-case perturbation scenario found under the grid control inputs' and state variables' constraints.

Furthermore, it is not uncommon to consider the AC side of the network as a stiff grid when the main focus of the research is on HVDC grids' stability, leading to neglecting the generator and its controls' dynamics and its harmonic interactions with the DC side of the grid. For instance, reference [18] proposes a single-input single-output (SISO) feedback control model of a hybrid dual-infeed HVDC system to quantitatively investigate the effect of the dynamic interactions between the AC grid strength and control parameters on the stability margins. The goal is to propose a practical design and control methodology for HVDC systems; however, it demands a number of analyses and extensive retuning. Furthermore, the AC grid is simulated as a voltage source behind series resistance and inductance, and the DC-side voltage and current are assumed to be constant. In [19], an analytical and effective strategy, named the inequality constraints-based method, is introduced to estimate the stability regions of the droop slopes in MMC-based multiterminal HVDC systems. This methodology can further be applied to find the optimal droop control parameters, but the paper only focuses on small disturbance stability at the equilibrium point. Moreover, the AC grid and HVDC cable models are simplified as a stiff grid and T-equivalent circuit, respectively. A control parameter optimization method based on the quadratic index and damping ratio characteristics is proposed in [20] to improve the small-signal stability and dynamic response of a point-to-point hybrid LCC-MMC HVDC system. The methodology is optimal based on the Monte Carlo approach but requires communications among converter stations. The AC grid here is represented through a voltage source behind series resistance and inductance, neglecting the generator and its controllers' dynamics. Reference [21] introduces a methodology for the optimal design of controller parameters to guarantee the small-signal stability of the interconnected MMC-HVDC grids for wind farm integration. The impedance-based analysis approach is used to retune the AC voltage controller optimally, and there are a number of simplifications in grid modelling, including the AC grid represented as a constant power source. The controller parameters' optimization is also investigated in [22] to maximize the phase margin of the MMC-HVDC integrated system, considering the delay effect. An MMC impedance optimization method is proposed that traverses all the potential controllers' parameters' values within the derived boundaries to improve the high-frequency stability. Thus, the methodology can be complicated and time-consuming when the number of converter stations increases. Furthermore, the methodology applies simplifications in the AC grid and HVDC cable modelling.

1.1 | Motivation and contributions

According to the previous discussion on the most recent scientific works regarding the stability issues and dynamic interactions due to the interconnection and expansion of

MMC-based HVDC grids, it can be concluded that there is a demand for (1) accurate modelling of the multiterminal hybrid AC/DC grids with sufficient details on all components (e.g. the generator and its controllers, MMC and its controller, and HVDC cable) to investigate the control and dynamic interactions between/within the AC and DC subgrids, and (2) an analytical and optimal control methodology to improve the interconnected grid stability and minimize the oscillations caused by the poorly damped modes that are identified from the grid's detailed model. Hence, this paper's motivation is to focus on the abovementioned demands to guarantee the stability of the MMC-based multiterminal hybrid AC/DC grids under the worst-case perturbation scenario.

We have initially proposed an analytical methodology to derive a decentralized optimal controller with constraints on the grid control inputs and state variables, under the worst-case perturbation scenario, to minimize the DC voltage oscillations in MMC-based offshore multiterminal HVDC grids [23]. The optimization problem formulation is inspired by [24], in which the goal was to minimize the generator frequency deviations in AC grids using a centralized optimal controller. However, it has never been tested whether the optimization approach can be extended to hybrid AC/DC grids to improve the stability margins and minimize the oscillations caused by the poorly damped modes. Additionally, neither had the optimal controller performance been assessed under the exact worst-case perturbation scenario obtained from the optimization procedure, nor under fault conditions, as it was only validated under small disturbances. Moreover, the optimal controller parametric robustness has never been evaluated.

Consequently, within this context, the paper's primary contributions are:

- Investigating the poorly damped modes in an MMC-based multiterminal hybrid AC/DC grid. Such a grid is modelled in detail to account for the multiple sources of oscillations resulting from the dynamic interactions between/within the AC and DC subgrids. It is shown that the poorly damped modes responsible for oscillations have a high sensitivity to the power system stabilizer (PSS) and MMC droop controller tuning parameters on the AC- and converter-side of the grid, respectively. Moreover, it is revealed from the detailed model of the grid that the MMC arm capacitors can contribute to minimizing oscillations arising from the AC side of the grid. Such phenomena would have remained unnoticed if simplified models on either side of the grid were applied.

- Scrutinizing the applicability and feasibility of the decentralized optimal linear feedback controller to improve the stability margins and reduce oscillations under the worst-case perturbation/oscillation scenario and grid control inputs' and state variables' constraints. These oscillations are primarily caused by the poorly damped modes in MMC-based multiterminal hybrid AC/DC grids. To this end, the performance of the controller is validated under the following cases:
  ° worst-case perturbation/oscillation scenario,
  ° small and large disturbances (three-phase short circuit fault),

  ° absence or presence of the traditional PSS or MMC droop controller, and
  ° uncertainties in control parameters, grid parameters, and operating conditions.

Furthermore, a comparative analysis between this paper and the relevant abovementioned literature is presented in Table 1 to highlight the paper's contributions. The remainder of the paper is organized as follows: Section 2 presents the MMC-based multiterminal hybrid AC/DC grid under study and its associated state-space model, which is essential for the decentralized optimal controller's derivation and small-signal eigenvalue stability analysis. In Section 3, the decentralized optimal controller's problem formulation and implementation for minimizing the oscillations caused by the poorly damped modes of the grid under study are given. Section 4 analyses the small-signal eigenvalue stability for identifying the grid's poorly damped modes and investigates the performance of the decentralized optimal controller in improving damping ratios and stability margins of these modes. In Section 5, time-domain simulations are given to evaluate the decentralized optimal controller under small and large disturbances, in the presence or absence of the PSS and MMC droop controller, and under control parameters, grid parameters, and operating conditions uncertainties. The pros and cons, and scalability of the proposed methodology are discussed in Section 6. Finally, the conclusion is presented in Section 7.

2 | HYBRID AC/DC GRID UNDER STUDY

The system under analysis here is an MMC-based multiterminal hybrid AC/DC grid shown in Figure 1. It is a 14-bus system composed of three AC grids interconnected through an MMC-based three-terminal HVDC network. One of the AC grids containing G1 and G4 has two areas that are 50 km apart. Among the three converter stations, MMC1 and MMC3 are controlled via the DC-d

roop mode while MMC2 is in power mode control.

In this section, the grid's steady-state time-invariant (SSTI) state-space model is obtained as a prerequisite for implementing the decentralized optimal controller to improve the grid stability. It is also used for analysing the small-signal eigenvalue stability to identify the grid's poorly damped modes. The general form of the grid state-space model can be stated as [25]:

$$\dot{\boldsymbol{x}} = f(\boldsymbol{x}, \boldsymbol{u}), \quad \boldsymbol{z} = g(\boldsymbol{x}, \boldsymbol{u}), \tag{1}$$

where $\boldsymbol{x}$, $\boldsymbol{u}$, and $\boldsymbol{z}$ are defined as the grid state vector, control input vector, and output vector, respectively.

2.1 | State-space model of the AC grid

The AC grid parameters adapted from [25] are given in Table 2. The generators are represented based on the detailed

TABLE 1 Summary of the comparison between the proposed approach and other relevant references

Ref.	Methodology	A	B	C	D	E	F	G	H	I
This paper	Decentralized optimal linear feedback controller	✓	✓	✓	✓	✓	✓	✓	✓	✓
[13]	DC-side damper structure (impedance-based modelling)	✓	✗	✓	✗	✗	✓	✗	✗	✓
[14]	Feedback linearization technique	✓	✓	✗	✗	✗	✗	✗	✗	✗
[15]	Adaptive phase locked loop (PLL) controller	✓	✓	✗	✗	✗	✗	✗	✓	✗
[16]	Global model predictive control (MPC)-based grid controller	✗	✓	✗	✓	✓	✓	✗	✗	✗
[17]	Distributed supplementary control	✗	✓	✓	✗	✗	✗	✗	✗	✗
[18]	Single-input single-output (SISO) feedback control model	✓	✗	n.a.	n.a.	n.a.	✗	✓	✗	n.a.
[19]	Inequality constraints-based method for fast estimation of droop-slope stability regions	✗	✓	✓	✗	✓	✗	✓	✗	✓
[20]	Control parameter optimization based on quadratic index and damping ratio	✓	✓	✗	✓	✓	✗	✓	✗	✗
[21]	Impedance-based optimal design on controller parameters	✓	✗	n.a.	n.a.	n.a.	✗	✓	✗	n.a.
[22]	Modular multilevel converter (MMC)impedance optimization	✓	✗	n.a.	n.a.	n.a.	✗	✓	✗	n.a.
[24]	Linear feedback controller	✗	✓	✗	✓	✓	✗	✗	✗	✗

Note: A: Analysing control and dynamic interactions; B: Analytical methodology (no retuning or repetitive calculations or dynamic simulations); C: Decentralized controller; D: Optimal controller (under worst-case perturbation scenario); E: Under control inputs' and state variables' constraints (inequality constraints); F: AC-side detailed model (synchronous generator with controllers); G: Converter detailed model (MMC with controllers); H: DC-side detailed model (high-voltage direct current [HVDC] cable); I: Discussion on implementation feasibility (communication requirements, scalability).

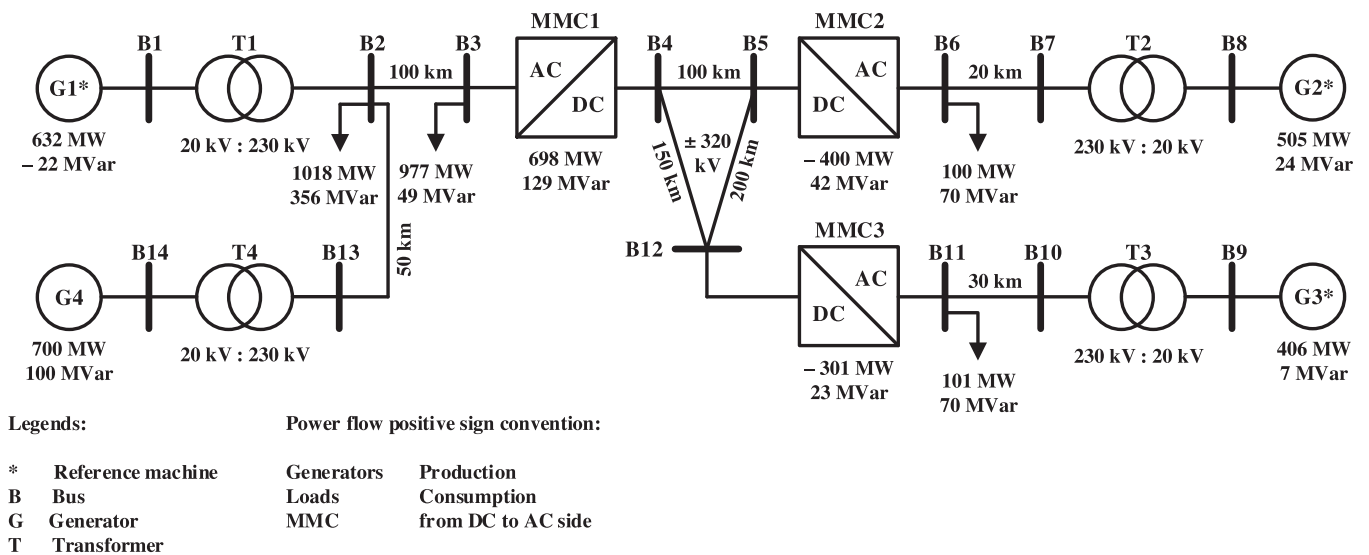Abbreviations: n.a., not applicable/available

FIGURE 1 Hybrid AC/DC grid under study

sixth-order model equipped with the AVR of the simplified excitation system type, hydro turbine governor (HTG) of the HYGOV type, and speed-sensitive PSS [25]. AC loads are considered as constant impedance (Z). Therefore, the state-space representation of the AC grid with the state vector, $\boldsymbol{x}_G$, and the control input vector, $\boldsymbol{u}_G$, for every generator can be stated as:

$$\boldsymbol{x}_G = [\psi_{fd}\ \psi_{1d}\ \psi_{1q}\ \psi_{2q}\ \omega_m\ \delta$$
$$\gamma_{avr1}\ \gamma_{avr2}\ \gamma_{htg1}\ \gamma_{htg2}\ \gamma_{htg3}\ \gamma_{htg4}\ \gamma_{pss1}\ \gamma_{pss2}]^T, \quad (2)$$

$$\boldsymbol{u}_G = [v_{avr}^*\ \omega_m^*]^T, \quad (3)$$

where ψ_{fd}, ψ_{1d}, ψ_{1q}, and ψ_{2q} are the per-unit rotor flux linkages. The state variables ω_m and δ are the rotor angular velocity and position, respectively. Moreover, γ is associated with the controller's integral state. The superscript * denotes the reference value, and v_{avr}^* and ω_m^* are the AVR reference voltage and HTG reference angular velocity, respectively. It is worth mentioning that the state variables γ_{pss1} and γ_{pss2} are valid for the reference generators G1, G2, and G3, and δ is only a state variable of G4.
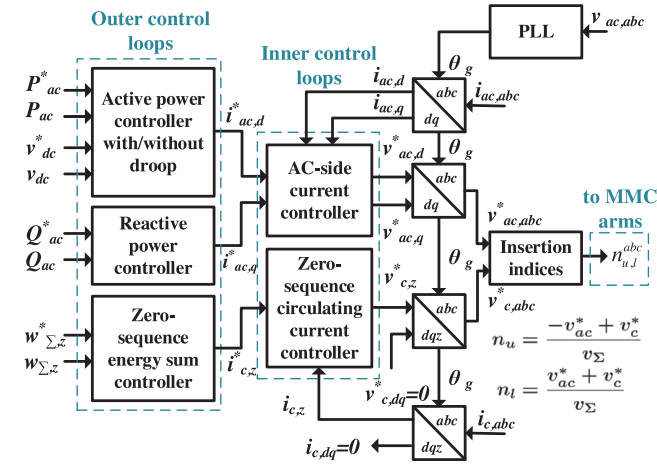
FIGURE 2 MMC topology and control

TABLE 2 AC grid parameters

Synchronous generator			
Parameter	**Value**	**Parameter**	**Value**
S_{rated}	900 MVA	V_{rated}	20 kV
R_a	0.0025 pu	X_l	0.2 pu
X_d	1.8 pu	X_q	1.7 pu
X_d'	0.3 pu	X_q'	0.55 pu
X_d''	0.25 pu	X_q''	0.25 pu
T_{d0}'	8 s	T_{q0}'	0.4 s
T_{d0}''	0.03 s	T_{q0}''	0.05 s
H_{G1}	7 s	H_{G2}	7 s
H_{G3}	6 s	H_{G4}	6 s
Transformer			
Parameter	**Value**	**Parameter**	**Value**
S_{rated}	900 MVA	X_t	0.15 pu
$V_{primary}$	20 kV	$V_{secondary}$	230 kV
AC transmission line			
Parameter	**Value**	**Parameter**	**Value**
S_{rated}	100 MVA	V_{rated}	230 kV
r_l	0.0001 pu/km	x_l	0.001 pu/km

TABLE 3 Modular multilevel converter (MMC) and high-voltage direct current (HVDC) cable parameters

MMC	
Parameter	**Value**
Base apparent power, S_b	900 MVA
Base DC voltage, V_b^{dc}	640 kV
Converter nominal AC voltage, V_{conv}^{ac}	380 kV
Frequency, ω	$2\pi 50$ rad/s
Arm resistance, R_a	0.885 Ω
Arm inductance, L_a	84.8 mH
Arm capacitance, $C_a = C_{SM}/N$	29.3 μF
Transformer resistance, R_t	1.77 Ω
Transformer reactance, X_t	17.7 Ω
DC link capacitance, C_{dcl}	219.74 μF

HVDC cable			
Parameter	**Value**	**Parameter**	**Value**
R_{dc1}	2.65 Ω/km	L_{dc1}	0.6016 mH/km
R_{dc2}	0.1218 Ω/km	L_{dc2}	0.302 mH/km
R_{dc3}	0.016 Ω/km	L_{dc3}	2.8 mH/km
C_{dc}	0.16 μF/km		

2.2 | State-space model of the MMC and HVDC cable

2.2.1 | MMC state-space model

The MMC model shown in Figure 2 with parameters [26] given in Table 3 is developed based on a simplified averaged model that is derived from the converter energy–based representation with compensated modulation (CM) [27]. The CM methodology compensates for the oscillations in the arm capacitor voltages by defining the insertion indices as the ratio of the refer-
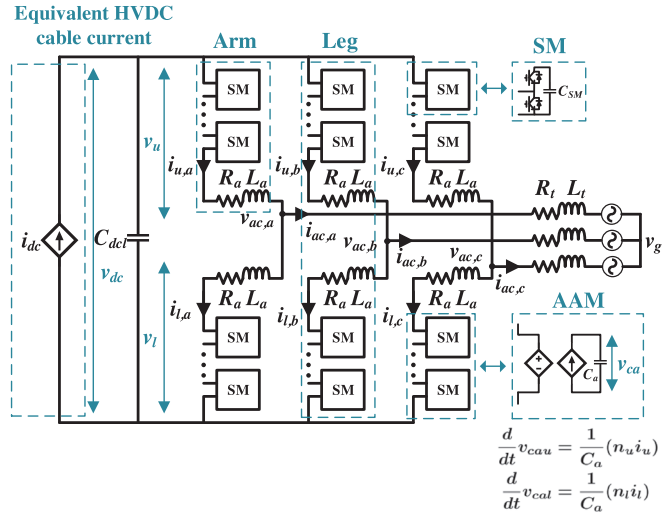
ence control voltages to the measured or estimated arm capacitor voltages [27]. Hence, the aggregated upper and lower arm capacitor voltages can be assumed to be balanced and represented as:

$$w_{ul} = \frac{1}{2} C_a v_{ca,ul}^2, \tag{4}$$

where w_{ul} and $v_{ca,ul}$ are the aggregated upper (u) and lower (l) arm capacitor energy and voltage ($v_{ca,ul} = \sum_{i=1}^{N} v_{SM,ul}$), respectively.

The MMC SSTI equations can be derived by decomposing the upper and lower arm insertion indices (n), currents (i), and voltages (v) into differential (ac) and common-mode (c) ones:

$$n_{ac} = \frac{n_l - n_u}{2} \qquad n_c = \frac{n_u + n_l}{2}, \tag{5}$$

$$i_{ac} = i_u - i_l \qquad i_c = \frac{i_u + i_l}{2}, \tag{6}$$

$$v_{ac} = \frac{v_l - v_u}{2} \qquad v_c = \frac{v_u + v_l}{2}, \tag{7}$$

where v_{ac} and i_{ac} are the AC-side voltage and current. The common-mode variable i_c is known as the circulating current and v_c is the voltage driving it.

Therefore, the MMC dynamics in rotating dqz reference frame can be written as:

$$\frac{d}{dt} i_{ac,dq} = \frac{1}{L_{ac}} (v_{ac,dq}^* - v_{g,dq} - R_{ac} i_{ac,dq} - j\omega L_{ac} i_{ac,dq}), \tag{8}$$

$$\frac{d}{dt} v_{dc} = \frac{1}{(C_{dcl} + \frac{C_{dc}}{2})} (i_{dc} - 3i_c), \tag{9}$$

$$\frac{d}{dt} i_c = \frac{1}{L_a} (\frac{v_{dc}}{2} - v_c^* - R_a i_c), \tag{10}$$

$$\frac{d}{dt} v_\Sigma = \frac{1}{C_a} (n_c^* i_c - \frac{1}{2} n_{ac}^* i_{ac}), \tag{11}$$

where $v_{g,dq}$ is the dq-component of the equivalent AC-side voltage, and v_{dc} and i_{dc} are the DC-side voltage and current, respectively. Moreover, $R_{ac} = R_t + R_a/2$ and $L_{ac} = L_t + L_a/2$. The variable v_Σ is given by $(v_{ca,u} + v_{ca,l})/2$. Thus, the reference insertion indices n_{ac}^* and n_c^* can be defined as v_{ac}^*/v_Σ and v_c^*/v_Σ, respectively.

Accordingly, the state-space representation of the MMC with the vectors $\boldsymbol{x_{mmc}}$ and $\boldsymbol{u_{mmc}}$, while considering the converter control topology shown in Figure 2, becomes:

$$\boldsymbol{x_{mmc}} = [i_{ac,d} \; i_{ac,q} \; v_{dc} \; i_c \; v_\Sigma$$
$$\xi_{iacd} \; \xi_{iacq} \; \xi_{pac} \; \xi_{qac} \; \xi_{icz} \; \xi_{w\Sigma z} \; \xi_{pll} \; \Theta_g]^T, \tag{12}$$

$$\boldsymbol{u_{mmc}} = [v_{dc}^* \; P_{ac}^* \; Q_{ac}^* \; w_{\Sigma,z}^*]^T, \tag{13}$$

where P_{ac} and Q_{ac} are the AC-side active and reactive powers, respectively. Additionally, $w_{\Sigma,z}$ is the zero-sequence energy sum that can be calculated as $w_{\Sigma,z} = w_u + w_l = \frac{1}{2} C_a (v_{ca,u}^2 + v_{ca,l}^2)$. The MMC control architecture (shown in Figure 2) is based on the conventional cascaded inner and outer control loops with PI controllers that are tuned using the modulus and symmetrical optimum techniques [28]. The variable ξ is related to the PI controllers' integral state, and Θ_g is the measured AC grid voltage angle detected by a PLL.

2.2.2 | HVDC cable state-space model

The HVDC cable with parameters given in Table 3 is represented based on the frequency-dependent model with one pi-section and three parallel series branches [29]. Hence, the state-space representation for every HVDC cable contains three current states as follows:

$$\boldsymbol{x_C} = [i_{dc,1} \; i_{dc,2} \; i_{dc,3}]^T. \tag{14}$$

It is worth mentioning that the effect of the cable shunt capacitance is considered in (9).

3 | DECENTRALIZED OPTIMAL CONTROLLER PROBLEM FORMULATION

A decentralized optimal linear feedback controller is introduced to minimize the oscillations caused by the poorly damped modes in the MMC-based multiterminal hybrid AC/DC grid. The optimal controller is obtained under the worst-case perturbation scenario while considering constraints on the control inputs and state variables fluctuations. The methodology for developing the optimal controller is initially taken from [24, 30], which is a non-convex min–max optimization problem converted into semidefinite programming (SDP) using the Lyapunov stability and linear matrix inequality (LMI) theories. The aim was to minimize the frequency deviation of the generators represented by the second-order model via a *centralized* optimal controller in AC grids. Namely, the grid stability was improved by placing HVDC links represented as complex current sources, in which the optimal controller manipulated their injected active and reactive currents.

We adapted the methodology to our objective to minimize the DC voltage oscillations in MMC-based multiterminal HVDC grids [23, 31]. Furthermore, the *centralized* optimal controller was developed to be *decentralized* or block-diagonal to match the grid sparsity pattern and eliminate the communication over long distances between converter stations. Furthermore, the constraints on the control inputs and state variables were decoupled, allowing for more practicality and tractability in design and control.

However, the performance of the decentralized optimal controller has never been investigated in hybrid AC/DC grids that are modelled in detail. Hence, the paper's main aim is to prove the effectiveness of a suitably extended decentralized optimal control approach in improving the grid stability margins and minimizing the oscillations under the worst-case perturbation scenario and decoupled constraints on the control inputs and state variables in MMC-based multiterminal hybrid AC/DC grids.

Therefore, an oscillation index, J_{osci}, is introduced to minimize the fluctuations caused by the poorly damped modes via the decentralized optimal controller, $\boldsymbol{K}$, under the worst-case

perturbation scenario, $\mathbb{X}_0$:

$$J_{osci} = \min_{K} \max_{x(0) \in \mathbb{X}_0} \int_0^\infty z(t)^T M z(t) \, dt \qquad (15)$$

$$\text{s.t. } \dot{x}(t) = Ax(t) + Bu(t), \qquad (16)$$

$$z(t) = Cx(t), \qquad (17)$$

$$u(t) = Kx(t), \qquad (18)$$

where

$$x(0) \in \mathbb{X}_0 = \{x_i \in \mathbb{R}^{n_i} : \quad \forall i \in \mathbb{Z}_{[1,r]} \ x_i^T E_x^i x_i \leq 1\}, \qquad (19)$$

$$u(t) \in \mathbb{U} = \{u_j \in \mathbb{R}^{m_j} : \quad \forall j \in \mathbb{Z}_{[1,q]} \ u_j^T E_u^j u_j \leq 1\}. \qquad (20)$$

The signals of interest, $z(t)$, whose oscillations we aim to minimize, are state variables linked to the poorly damped modes (as defined later in Section 4) and are weighted with the symmetric positive semidefinite matrix $M = \hat{M}\hat{M}^T \geq 0$. In the following section, the small-signal eigenvalue stability and participation factor analysis are performed to distinguish the most dominant modes with the lowest damping ratios and their corresponding participating state variables to minimize their oscillations. Matrices $A \in \mathbb{R}^{n \times n}$, and $B \in \mathbb{R}^{n \times m}$ are the grid state-space matrices found according to the grid overall state variables, x, and control inputs, u:

$$x = \begin{bmatrix} x_{G1}^T & x_{G4}^T & x_{mmc1}^T & x_{C12}^T & x_{G2}^T \\ & & & & \\ x_{mmc2}^T & x_{C23}^T & x_{G3}^T & x_{mmc3}^T & x_{C13}^T \end{bmatrix}^T, \qquad (21)$$

$$u = \begin{bmatrix} u_{G1}^T & u_{G4}^T & u_{mmc1}^T & u_{G2}^T u_{mmc2}^T & u_{G3}^T & u_{mmc3}^T \end{bmatrix}^T, \qquad (22)$$
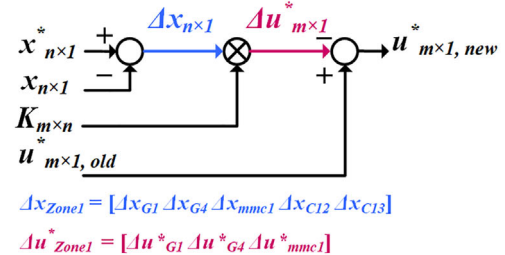
where $n = 99$ and $m = 19$.

The decentralized optimal linear feedback controller, K, architecture, and implementation (18) are depicted in Figure 3. As can be seen from the figure, the decentralized optimal controller is block-diagonal with three separate control zones to avoid the necessity for communication among converter stations over long distances. Namely, the state variables' variations (Δx_i), which can be measured or estimated through wide-area measurement systems (WAMS), are sent to their associated optimal controller block ($K1$, $K2$, or $K3$), and the resultant reference inputs' variations of the generators and MMCs control loops (Δu_j^*) are transferred only to their corresponding control zones (Zone1, Zone2, or Zone3).

The optimization objective (15) is subject to decoupled ellipsoidal constraints on the state variables (19) and control inputs (20), which are defined using the symmetric positive definite matrices $E_x^i > 0$ and $E_u^j > 0$. Accordingly, r and q are the
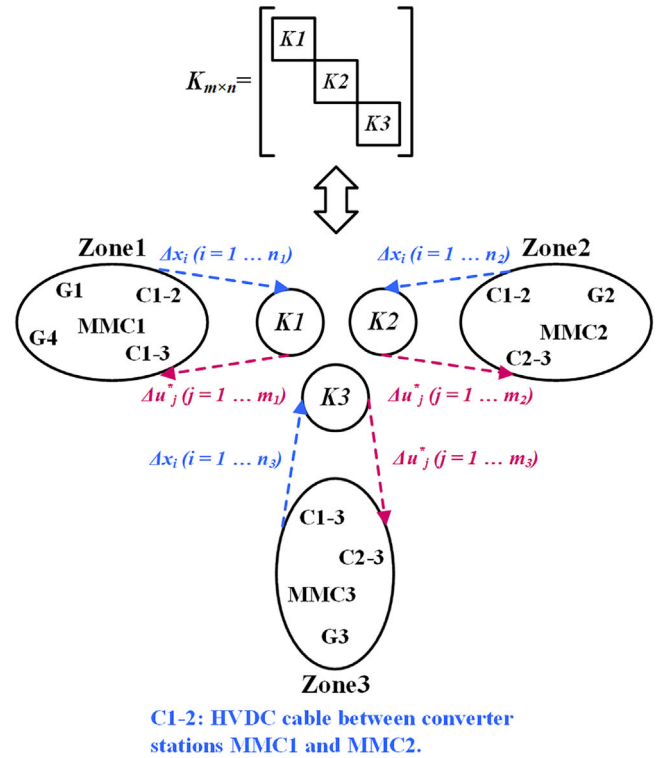
(a) Decentralized (block-diagonal) optimal controller architecture.

$\Delta x_{Zone1} = [\Delta x_{G1} \ \Delta x_{G4} \ \Delta x_{mmc1} \ \Delta x_{C12} \ \Delta x_{C13}]$

$\Delta u^*_{Zone1} = [\Delta u^*_{G1} \ \Delta u^*_{G4} \ \Delta u^*_{mmc1}]$

(b) Decentralized optimal controller implementation.

FIGURE 3 Decentralized optimal linear feedback controller architecture and implementation

total number of the ellipsoidal constraints on the state variables and control inputs, respectively ($r = 10$ and $q = 16$). Thus, $\sum_{i=1}^r n_i = n$ and $\sum_{j=1}^q m_j = m$. Namely, the decentralized optimal controller, K, aims to minimize the maximum possible amount of the oscillations under the worst-case perturbation scenario, $\mathbb{X}_0$, found under the small-signal approximations defined by (19) and (20). The feasibility of implementing decoupled constraints on the state variables and control inputs improves the optimal controller flexibility based on the design requirements.

For instance, the decoupled ellipsoidal constraints on the state variables (20) of the hybrid AC/DC grid, which are defined based on Figure 3a, are such that a 10% limit is applied on the square root of the sum of the squares of the disturbances for every piece of grid equipment (every generator, MMC, and HVDC cable such that $r = 10$), describing the search area for

the expected worst-case perturbation scenario:

$$\left(\Delta\psi_{fd}^2 + \Delta\psi_{1d}^2 + \Delta\psi_{1q}^2 + \Delta\psi_{2q}^2 + \Delta\omega_m^2 + \Delta\delta^2 + \right.$$
$$\Delta\gamma_{avr1}^2 + \Delta\gamma_{avr2}^2 + \Delta\gamma_{htg2}^2 + \Delta\gamma_{htg3}^2 +$$
$$\left. \Delta\gamma_{htg4}^2 + \Delta\gamma_{pss1}^2 + \Delta\gamma_{pss2}^2 \right)^{1/2} \leq 0.1 \text{ pu}, \qquad (23)$$

$$\left(\Delta i_{ac,d}^2 + \Delta i_{ac,q}^2 + \Delta v_{dc}^2 + \Delta i_c^2 + \Delta v_\Sigma^2 + \right.$$
$$\Delta\xi_{iacd}^2 + \Delta\xi_{iacq}^2 + \Delta\xi_{pac}^2 + \Delta\xi_{qac}^2 + \Delta\xi_{ic z}^2 +$$
$$\left. \Delta\xi_{w\Sigma z}^2 + \Delta\xi_{pll}^2 + \Delta\Theta_g^2 \right)^{1/2} \leq 0.1 \text{ pu}, \qquad (24)$$

$$\left(\Delta i_{dc1}^2 + \Delta i_{dc2}^2 + \Delta i_{dc3}^2 \right)^{1/2} \leq 0.1 \text{ pu}. \qquad (25)$$

Hence, (23)–(25) resulted from (20) and are associated with the decoupled ellipsoidal constraints on every generator, MMC, and HVDC cable, respectively. The 0.1 pu can be implemented in the optimization problem formulation by defining the symmetric positive definite matrices E_x^i as diagonal with all their entries equal to 100. It is worth mentioning that these decoupled ellipsoidal constraints, which impose a variation limit for a group of state variables, can be modified and grouped differently based on the prescriptions of the relevant grid codes and standards.

On the other hand, the decoupled ellipsoidal constraints on the control inputs' variations for every generator and MMC resulting in $q = 16$, are defined as follows:

$$|\Delta v_{avr}^*| \leq 1 \text{ pu}, \qquad (26)$$

$$|\Delta\omega_m^*| \leq 1 \text{ pu}, \qquad (27)$$

$$|\Delta v_{dc}^*| \leq 1 \text{ pu}, \qquad (28)$$

$$\left((\Delta P_{ac}^*)^2 + (\Delta Q_{ac}^*)^2 \right)^{1/2} \leq 1 \text{ pu}, \qquad (29)$$

$$|\Delta w_{\Sigma z}^*| \leq 1 \text{ pu}. \qquad (30)$$

The 1 pu variation limit is selected to allow a high degree of freedom to the decentralized optimal controller to readjust the control inputs to reduce the oscillations caused by the poorly damped modes. Accordingly, the symmetric positive definite matrices E_u^j are defined as diagonal matrices with all their entries equal to 1.

Since the above optimization problem (15)–(20) is nonconvex in its objective and constraints, it is not straightforward to obtain its optimal solution. However, as shown in [23], it is possible to approximate it as a convex SDP problem using the

Lyapunov stability and LMI theories such that $J_{osci} \leq \tilde{J}_{osci}$:

$$\frac{1}{\tilde{J}_{osci}} = \max_{s_i>0, Q_i>0, Y, w, y_i} w \qquad (31)$$

$$\text{s.t.} \begin{bmatrix} (AQ + BY) + (AQ + BY)^T & QC^T \\ CQ & -I \end{bmatrix} \leq 0, \qquad (32)$$

$$\begin{bmatrix} Q & Y_j^T \\ Y_j & \frac{w}{r}(E_u^j)^{-1} \end{bmatrix} \geq 0, \quad \forall j \in \mathbb{Z}_{[1,q]}, \qquad (33)$$

$$Q_i - s_i(E_x^i)^{-1} \geq 0, \quad \forall i \in \mathbb{Z}_{[1,r]}, \qquad (34)$$

$$\left\| \begin{matrix} 2w \\ s_i - y_i \end{matrix} \right\|_2 \leq s_i + y_i, \quad \forall i \in \mathbb{Z}_{[1,r]}, \qquad (35)$$

$$\sum_{i=1}^r y_i = rw, \quad Q = \text{blkdiag}(Q_i), \qquad (36)$$

$$Y = \text{blkcol}(Y_i), \quad Y \text{ is decentralized}, \qquad (37)$$

where w is a decision variable defined via an upper bound such that $w \leq (r/\sum_{i=1}^r (1/s_i))$, and is proportional to a scalar quantity, $s_i > 0$, $\forall i \in \mathbb{Z}_{[1,r]}$. Hence, the optimization objective (31) entails a convex formulation by maximizing w, which minimizes the oscillations caused by the poorly damped modes. The convex representation of the w and s_i derivations are stated through a set of decision variables $y_i > 0$, $\forall i \in \mathbb{Z}_{[1,r]}$ as given in (35) and (36). Equation (32) enforces the Lyapunov stability with the symmetric positive definite matrix $P > 0$ as the unique solution, in which it is block-diagonal with dimensions $n_i \times n_i$ on its i-th block $P_i = Q_i^{-1}$. Since matrix $Q = \text{blkdiag}(Q_i)$ is block-diagonal, if matrix $Y = \text{blkcol}(Y_i)$ has the desired decentralized structure, then the optimal controller $K = YQ^{-1}$ inherits the same structure. Furthermore, by using the Schur complement, the decoupled ellipsoidal constraints on the state variables (19) and control inputs (20) are reformulated in the convex form of (34) and (33), respectively.

The worst-case perturbation scenario, $x_{0,worst}$, is derived as $\hat{E}_x^{i(-T)} v_1$, where $E_x^i = \hat{E}_x^i \hat{E}_x^{iT}$ and $\hat{E}_x^i = V_x^i D_x^{i\frac{1}{2}}$ so that V_x^i contains the right eigenvectors of E_x^i, D_x^i is diagonal with the eigenvalues of E_x^i, and v_1 is the right eigenvector of $\hat{E}_x^{i(-1)} Q_i^{-1} \hat{E}_x^{i(-T)}$ corresponding to its largest eigenvalue.

The interested reader is referred to [23] for more details on definitions and derivations of (31)–(37) since they are not the main focus of the paper.

Eventually, the decentralized optimal controller problem formulation, (31)–(37), can be solved using the YALMIP optimization toolbox [32] of MATLAB in conjunction with the MOSEK solver [33] that is an interior-point optimizer for linear, quadratic, and conic problems.
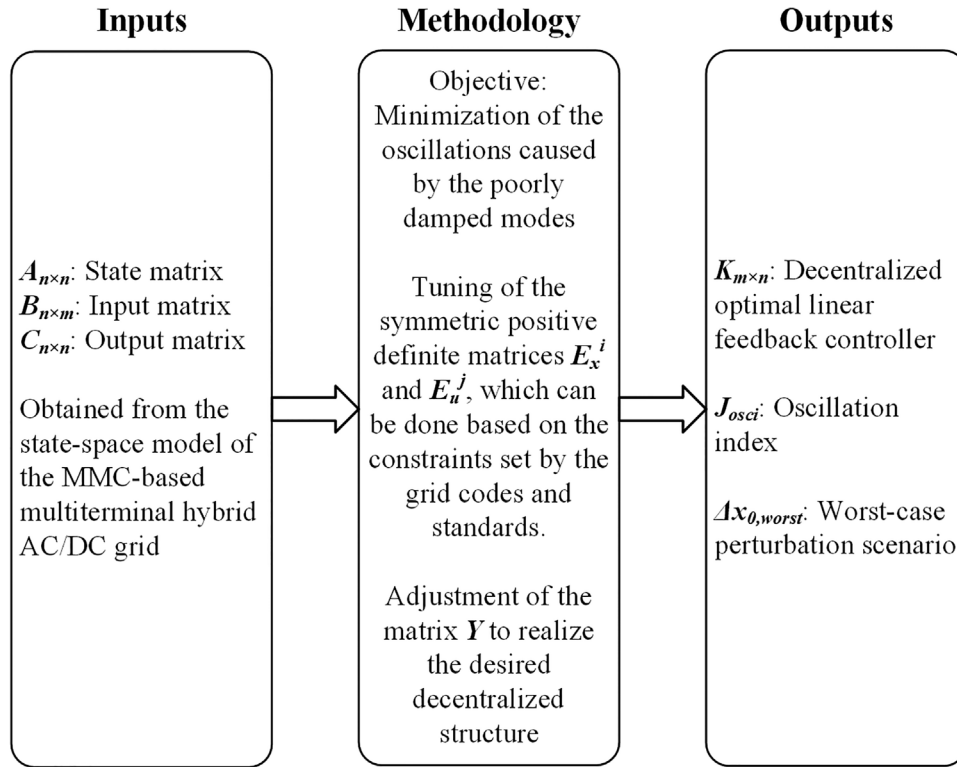
Inputs

Methodology

Outputs

$A_{n \times n}$: State matrix
$B_{n \times m}$: Input matrix
$C_{n \times n}$: Output matrix

Obtained from the state-space model of the MMC-based multiterminal hybrid AC/DC grid

Objective: Minimization of the oscillations caused by the poorly damped modes

Tuning of the symmetric positive definite matrices E_x^i and E_u^j, which can be done based on the constraints set by the grid codes and standards.

Adjustment of the matrix Y to realize the desired decentralized structure

$K_{m \times n}$: Decentralized optimal linear feedback controller

J_{osci}: Oscillation index

$\Delta x_{0,worst}$: Worst-case perturbation scenario

FIGURE 4 The optimization methodology with its inputs and outputs

3.1 | Optimization methodology interpretation

The optimization methodology with its inputs and outputs is presented in Figure 4.

The inputs to the optimization procedure are matrices $A_{99 \times 99}$, $B_{99 \times 19}$, and $C_{99 \times 99}$. The matrices $A_{99 \times 99}$ and $B_{99 \times 19}$ can be found by linearizing the grid state-space model around its operating point. Further, the diagonal matrix $C_{99 \times 99}$ that is representative of the state variables associated with the poorly damped modes can be found from the small-signal eigenvalue stability analysis. More details on the derivation of these three matrices are given in the following section.

The optimization objective is the minimization of the oscillations caused by the poorly damped modes (refer to Section 4) via the decentralized optimal linear feedback controller under the worst-case perturbation scenario (refer to (15)). This worst-case scenario, $\Delta x_{0,worst}$, is obtained under the decoupled ellipsoidal constraints on the state variables and control inputs. The symmetric positive definite matrices E_x^i and E_u^j can be tuned to define the limits on the ellipsoidal constraints as depicted in the previous section. The outputs of the optimization methodology are sensitive to these two matrices, E_x^i and E_u^j, which should be reasonably and sensibly selected. Moreover, the desired decentralized structure of the controller (shown in Figure 3a,) can be realized by adjusting the relevant entries of the matrix Y to zero.

The outputs from the optimization procedure are the decentralized optimal controller ($K_{m \times n}$), the oscillation index (J_{osci}),

and the worst-case perturbation scenario ($\Delta x_{0,worst}$). The oscillation index is the objective to be minimized by the optimization process and is representative of the amount of the oscillations caused by the poorly damped modes. This index can be further applied as a potential stability decision-support criterion in transmission expansion planning (TEP).

4 | SMALL-SIGNAL EIGENVALUE STABILITY ANALYSIS

The small-signal eigenvalue stability analysis is carried out for the MMC-based multiterminal hybrid AC/DC grid to serve three primary purposes: first, to gain a better insight into the grid stability and dynamics; second, to find the grid's poorly damped modes; and third, to evaluate the decentralized optimal controller's performance to improve the damping ratio of the poorly damped modes and grid stability margins.

The state-space model of the grid obtained in Section 2 is linearized around the operating point depicted by the power flow condition in Figure 1. Hence, the matrices $A_{99 \times 99}$ and $B_{99 \times 19}$ that are among the inputs of the optimization procedure are obtained. Time-domain verification is used to validate the accuracy of the linearized model by comparing it with the circuit-based (component-based) model developed in MATLAB/Simulink via the Simscape toolbox. The results are shown in Figure 5. A 1% step increase is applied to G1 reference rotor angular velocity at $t = 1$, and ω_m waveforms of the generators

|
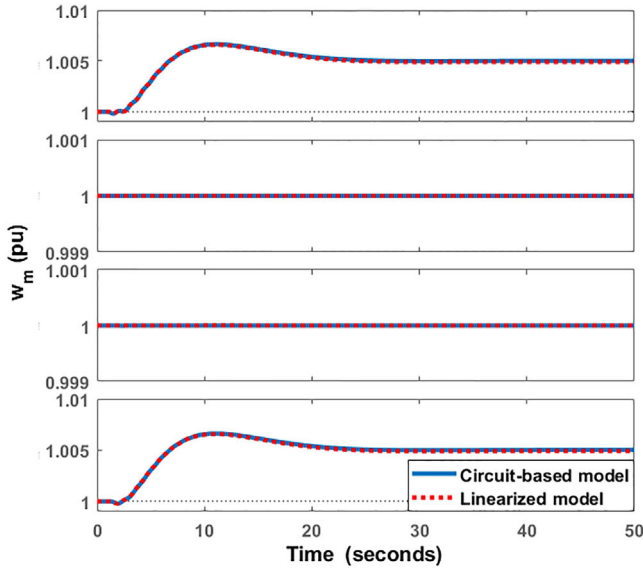
(a) Rotor angular velocity, w_m, of the generators G1, G2, G3, and G4 (from top to bottom).
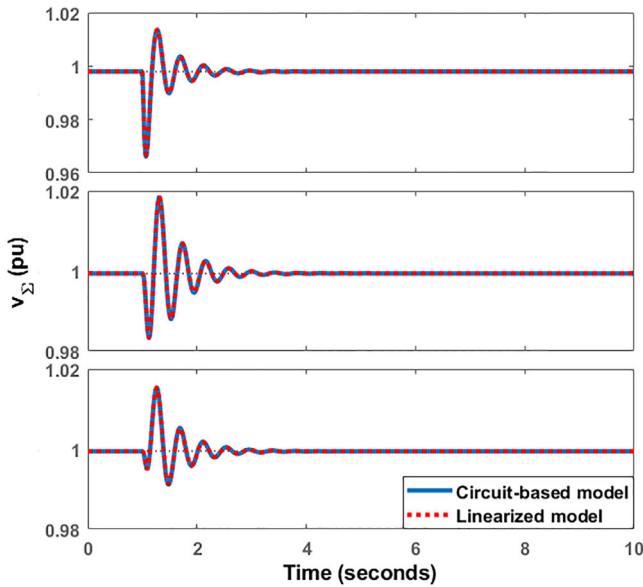
(b) Arm capacitor voltage, v_Σ, of the converters MMC1, MMC2, and MMC3 (from top to bottom).

FIGURE 5 Time-domain verification of the circuit-based model and linearized model of the MMC-based hybrid AC/DC study grid: (a) After applying a 1% step increase to G1 reference rotor angular velocity at $t = 1$ s, and (b) after applying a 10% step increase to MMC1 reference active power at $t = 1$ s

are given in Figure 5a. Next, Figure 5b demonstrates the MMC arm capacitor voltages after a 10% step increase of P_{ac1}^* at $t = 1$. The simulation results show that the two models match quite well, and the linearized model can accurately represent the grid dynamics under the transients.

Two pairs of poorly damped modes are identified through the small-signal eigenvalue stability analysis as given in Table 4. The first pair, $\lambda_{1,2}$, is defined as an electromechanical mode since its damping ratio is less than 5%, and its frequency is in the range
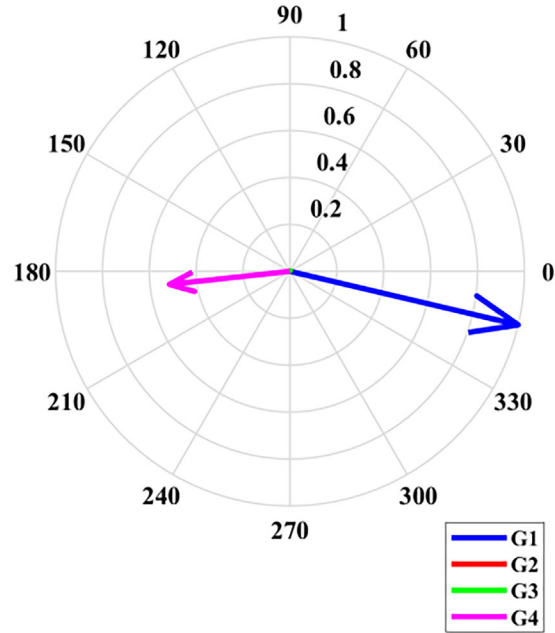
FIGURE 6 Observability (mode shape) of $\lambda_{1,2}$ in rotor angular velocity states of the generators

of 0.2–2 Hz. Participation factor analysis demonstrates that the state variables δ_4, w_{m1}, and w_{m4}, which are associated with G1 and G4, are the main contributors to this mode. Thus, Figure 6 indicates the relative observability of this mode in rotor angular velocity state variables of the generators when $\lambda_{1,2}$ is excited. It is evident from the figure that $\lambda_{1,2}$ is an inter-area mode with G1 and G4 oscillating against each other. On the other hand, the second pair of the poorly damped modes, $\lambda_{3,4}$, with damping ratio of 14%, is mainly affected by the MMC state variables $v_{\Sigma 2}$, $v_{\Sigma 1}$, $v_{\Sigma 3}$, $\xi_{w\Sigma z2}$, $\xi_{w\Sigma z1}$, and $\xi_{w\Sigma z3}$. This eigenvalue pair is categorized as a poorly damped mode since it has a low damping ratio as well as a high sensitivity to parametric variations, as shown in Figure 7b. That is, $\lambda_{1,2}$ is primarily influenced by the state variables on the generator-side of the grid, whereas the converter-side state variables are responsible for $\lambda_{3,4}$ properties.

Eigenvalue trajectory analysis is performed to investigate the sensitivity of the poorly damped modes to control parameters. It is found that $\lambda_{1,2}$ are very sensitive to PSS1 gain while the droop coefficient plays a pivotal role in $\lambda_{3,4}$ characteristics. It can be seen from Figure 7a that by increasing the PSS1 gain from 0.001 to 100, the system becomes unstable since $\lambda_{1,2}$ move towards the right half-plane. Similarly, the stability margins of $\lambda_{3,4}$ reduce as the MMC1 droop coefficient increases from 0.05 to 1 as presented in Figure 7b.

Now that the poorly damped modes and their corresponding state variables are identified, the decentralized optimal controller can be formulated such that:

$$z = [w_{m1} \quad w_{m4} \quad \delta_4 \quad v_{\Sigma 1}$$

$$w_{m2} \quad v_{\Sigma 2} \quad w_{m3} \quad v_{\Sigma 3}]^T. \tag{38}$$

TABLE 4   Poorly damped eigenvalues and their primary participating states

	Modular multilevel converter (MMC)-based hybrid AC/DC grid under study			
No.	**Eigenvalue (mode)**	**Damping ratio (%)**	**Frequency (Hz)**	**Main participating states[a]**
$\lambda_{1,2}$	$-0.27 \pm j\,5.46$	5	0.87	δ_4, w_{m1}, w_{m4}
$\lambda_{3,4}$	$-2.13 \pm j\,14.89$	14	2.37	$v_{\Sigma2}, v_{\Sigma1}, v_{\Sigma3}, \xi_{w\Sigma z2}, \xi_{w\Sigma z1}, \xi_{w\Sigma z3}$
	After addition of the decentralized optimal controller			
No.	**Eigenvalue (mode)**	**Damping ratio (%)**	**Frequency (Hz)**	**Main participating states[a]**
$\lambda_{1,2}$	$-0.67 \pm j\,5.69$	11.7	0.91	δ_4, w_{m1}, w_{m4}
$\lambda_{3,4}$	$-10.54 \pm j\,15.31$	56.7	2.44	$v_{\Sigma2}, v_{\Sigma1}, v_{\Sigma3}, \xi_{w\Sigma z2}, \xi_{w\Sigma z1}, \xi_{w\Sigma z3}$

aIndices 1, 2, 3, and 4 refer to generator G1, G2, G3, or G4 or converter MMC1, MMC2, or MMC3.
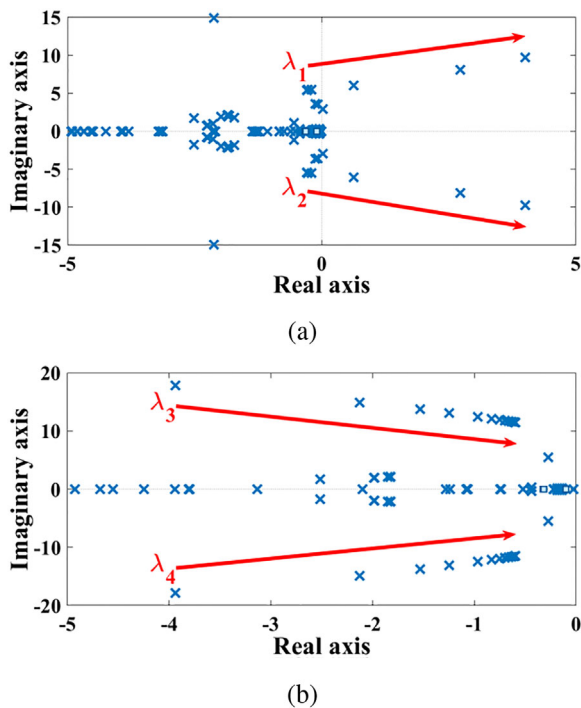
FIGURE 7   Eigenvalue trajectory for: (a) PSS1 gain variation from 0.001 to 100, (b) MMC1 droop variation from 0.05 to 1

Therefore, the optimization objective is to minimize the oscillations corresponding to the output vector's state variables, $z(t)$, under the worst-case perturbation scenario, to improve the damping ratios and stability margins of the poorly damped modes, $\lambda_{1,2}$ and $\lambda_{3,4}$. Hence, the matrix $\boldsymbol{C}_{99\times99}$ from (17) can be defined to be diagonal with weights on the entries corresponding to the state variables of the matrix $z(t)$. Namely, the worst-case perturbation scenario that is defined under the optimization constraints (19) and (20) yields the maximum oscillations associated with the state variables (38), which belong to both the AC- and DC side of the grid. The effect of the decentralized optimal controller on the poorly damped modes is summarized in Table 4. Evidently, $\lambda_{1,2}$ has moved from -0.27 to -0.67 with a slight change of frequency, which has improved the damping ratio from 5% to 11.7% (2.34 times). Likewise, the damp-

ing ratio of $\lambda_{3,4}$ has increased by a factor of 4.05 (from 14% to 56.7%), and the mode has further moved to the left from -2.13 to -10.54 (4.94 times).

5 | TIME-DOMAIN ANALYSIS

In this section, time-domain simulations are performed in MATLAB/Simulink to investigate the applicability of the decentralized optimal linear feedback controller under four different case studies. Its performance is compared with the PSS and MMC droop controller, representing the state-of-the-art solutions for the considered application, since the poorly damped modes, $\lambda_{1,2}$ and $\lambda_{3,4}$, are highly sensitive to these two controllers' tuning parameters, as shown in the previous section.

In the first case study, generator and converter control inputs are perturbed under different scenarios to evaluate the optimal controller performance under small disturbances. In the second case study, the worst-case perturbation scenario found under the optimization constraints is simulated, as the optimal controller performance has never been tested when the exact worst-case condition is modelled. Then, in the third case study, a three-phase short circuit, which is the worst type of fault [34], is applied on the AC side of the grid to explore the optimal controller performance under a large disturbance. Finally, the fourth test evaluates the optimal controller robustness against uncertainties in control parameters, grid parameters, and operating conditions.

5.1 | Case Study I

The purpose of this study is to evaluate the dynamic behaviour of the decentralized optimal controller when it is subject to perturbations (small disturbances) on the generator-side (exciting the mode $\lambda_{1,2}$) or converter-side of the grid (exciting the mode $\lambda_{3,4}$). To this end, the optimal controller performance is analysed when it is implemented into the grid operating under the condition explained in Section 2 together with scenarios where the PSS or droop controller is deactivated:
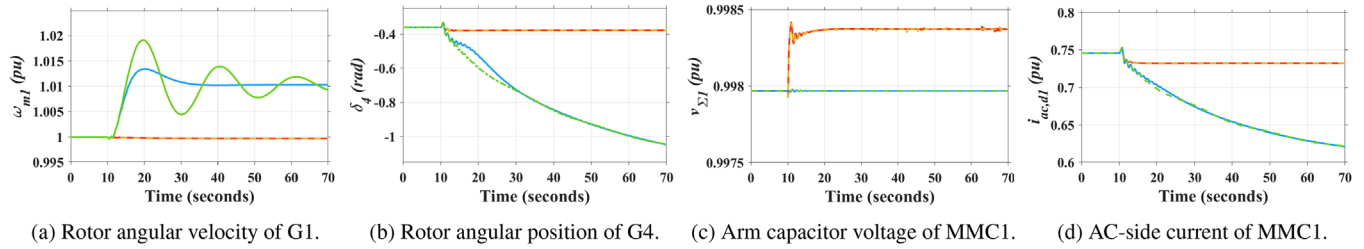
(a) Rotor angular velocity of G1. (b) Rotor angular position of G4. (c) Arm capacitor voltage of MMC1. (d) AC-side current of MMC1.

FIGURE 8 Decentralized optimal controller performance after applying a 2% step increase to G1 reference rotor angular velocity at $t = 10$ s: (yellow) with decentralized optimal controller only, (blue) with PSS1 only, (red) with both decentralized optimal controller and PSS1, and (green) without both decentralized optimal controller and PSS1
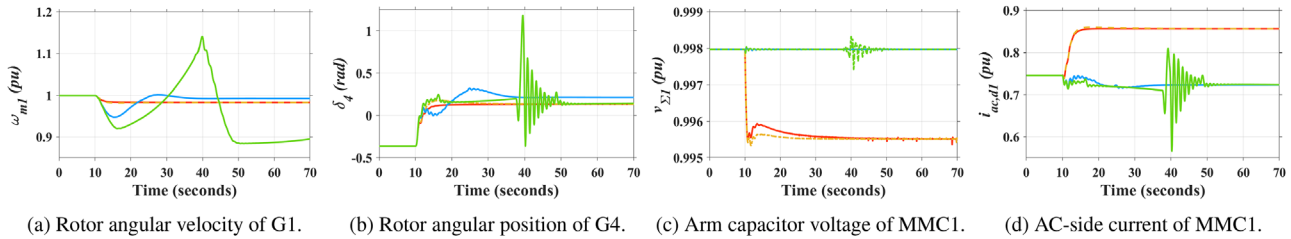

(a) Rotor angular velocity of G1. (b) Rotor angular position of G4. (c) Arm capacitor voltage of MMC1. (d) AC-side current of MMC1.

FIGURE 9 Decentralized optimal controller performance after applying a 20% step increase to G1 reference AVR voltage at $t = 10$ s: (yellow) with decentralized optimal controller only, (blue) with PSS1 only, (red) with both decentralized optimal controller and PSS1, and (green) without both decentralized optimal controller and PSS1

5.1.1 | Perturbations on the generator side

First, a 2% step increase is applied at $t = 10$ s to G1 reference rotor angular velocity, ω_{m1}^*, which is the reference input to the HTG1 and PSS1. Simulation results are depicted in Figure 8. It is apparent from the figure that when the decentralized optimal controller is implemented, either in the presence or absence of the PSS1, it is capable of limiting the ω_{m1} and δ_4 variations to a great extent, improving the damping of the mode $\lambda_{1,2}$. The controller has done this by exploiting the converter storage capacity through slightly increasing the $v_{\Sigma1}$ (0.04%), which results in the slight reduction of the MMC1 active power by 1.5%. In the absence of the decentralized optimal controller and when the PSS1 is active, the 2% step increase of the ω_{m1}^* results in a considerable decrease of the δ_4 and $i_{ac,d1}$, which substantially reduces the amount of active power delivered to the MMC1 (-15%). It should be noted that on this condition, the δ_4 and $i_{ac,d1}$ settle at new operating points after approximately 170 s and 110 s, respectively.

Second, the G1 reference AVR voltage, v_{avr1}^*, is increased by 20% at $t = 10$ s, and the results are shown in Figure 9. It is apparent from the figure that the ω_{m1} and δ_4 settling time is much shorter in the presence of the decentralized optimal controller than in its absence, and their oscillations are better damped. This fast response is obtained at the cost of a 0.3% decrease of the MMC1 arm capacitor voltage and an 11% increase of the MMC1 d-component current. When both the decentralized optimal controller and PSS1 are deactivated, the waveforms contain oscillations, and the grid eventually becomes unstable after about 110 s.

Overall, it can be observed that when the perturbations occur on the generator-side of the grid (exciting the mode $\lambda_{1,2}$), the decentralized optimal controller can operate even in the absence of the PSS1. Further, it can take up the PSS role in damping the oscillations more effectively and quickly by manipulating the converter storage capacity. In other words, the optimal controller performance is not dependent on the PSS1. Even if the PSS is absent or poorly tuned, the optimal controller can guarantee grid stability when the poorly damped electromechanical modes are excited.

5.1.2 | Perturbations on the converter side

First, a 20% step increase is applied to the MMC1 reference AC-side active power, P_{ac1}^*, at $t = 10$ s to excite the mode $\lambda_{3,4}$. According to Figure 10 the grid becomes unstable if there is no droop or decentralized optimal controller. The simulation results for the other scenarios are demonstrated in Figure 11. When there is only MMC1 droop control gain of 0.1 without the decentralized optimal controller, waveforms contain a high amount of oscillations at the frequency related to the mode $\lambda_{3,4}$, and the perturbation of P_{ac1}^* has resulted in the δ_4 on the generator-side varying from -0.36 to -0.38 rad. In the scenario with the decentralized optimal controller and droop, the oscillations are significantly reduced, and there is almost no oscillation when the optimal controller is operating without any droop controller on MMC1.

Second, the MMC1 reference zero-sequence energy sum, $w_{\Sigma,z1}^*$, is increased by 20% at $t = 10$ s, and the grid becomes
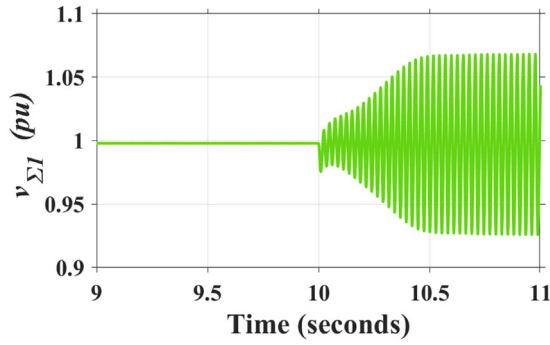
FIGURE 10   MMC1 arm capacitor voltage after applying a 20% step increase to MMC1 reference AC-side active power at $t = 10$ s when MMC1 droop control is deactivated

Control input	Variation	Control input	Variation
Δv_{avr1}^{*}	0.2	ΔQ_{ac1}^{*}	0.57
$\Delta \omega_{m1}^{*}$	0.4	Δv_{avr2}^{*}	0.3
Δv_{avr4}^{*}	0.67	ΔQ_{ac2}^{*}	0.36
$\Delta \omega_{m4}^{*}$	0.28	$\Delta v_{\Sigma2}^{*}$	−0.44

*Indices 1, 2, 3, and 4 refer to generator G1, G2, G3, or G4 or converter MMC1, MMC2, or MMC3.

unstable in the absence of the decentralized optimal controller and droop controller on MMC1. The results are given in Figure 12. As shown in the figure, waveforms fluctuate considerably at the frequency related to the mode $\lambda_{3,4}$ under the droop controller alone, and the oscillations decrease significantly when the decentralized optimal controller is operating either alone or together with the droop controller on MMC1.

Therefore, the decentralized optimal controller can efficiently damp the oscillations caused by the small perturbations on the converter-side of the grid (exciting the mode $\lambda_{3,4}$), whether the droop controller on the MMC1 is active or not. The optimal controller is not sensitive to the droop controller gain, which is an advantage in the case of poor tuning of the droop controllers in multiterminal configurations.

5.2 | Case Study II: Worst-case perturbation scenario

In this study, the performance of the decentralized optimal controller is tested for the first time against the worst-case perturbation scenario obtained from the optimization procedure. The worst-case perturbation is found under the constraints defined in (19), (20), (23)–(25), and (26)–(30). Table 5 depicts the primary control inputs' variations ($\geq$ 20%), which are associated with the worst-case perturbation scenario, $x_{0,worst}$. Simulation results are shown in Figure 13. Without the decentralized optimal controller, and in the presence of PSS and MMC droop controller, the grid becomes unstable (see Figure 13d at $t = 16$ s.)

under the worst-case perturbation scenario while the oscillations are within the frequency range related to the mode $\lambda_{1,2}$ (see Figure 13c and Figure 13d). On the other hand, the decentralized optimal controller (in the presence of PSS and MMC droop controller) can keep the system stable and damp the oscillations, such that the grid waveforms settle at a new operating point. It is worth mentioning that the grid power-sharing control is out of the scope of this paper, and it can further be managed by the grid's secondary controller at a higher level.

Consequently, the decentralized optimal controller can ensure the grid's stability under a higher range of dynamics and transients than the conventional grid controllers. Moreover, the optimal controller's applicability is validated under the condition claimed by the optimization results.

5.3 | Case Study III: Three-phase short circuit fault

In this section, the optimal controller performance under a large disturbance is investigated, which is beyond the optimization scope based on the small-signal approximation. A three-phase short circuit fault is applied at bus B2 at $t = 10$ s and cleared after 500 ms. The fault is used to excite the inter-area mode $\lambda_{1,2}$ on the AC side of the grid. The time-domain simulation results are demonstrated in Figure 14. The figure shows that the ω_{m1} and δ_4 waveforms, which are oscillating at the frequency related to the mode $\lambda_{1,2}$, settle in a much shorter time under the decentralized optimal controller. Figure 15 is given to show the ω_{m1} waveform under the same fault at a higher fictitious clearing time of 5 s. It is evident from the figure that the decentralized optimal controller can significantly reduce the
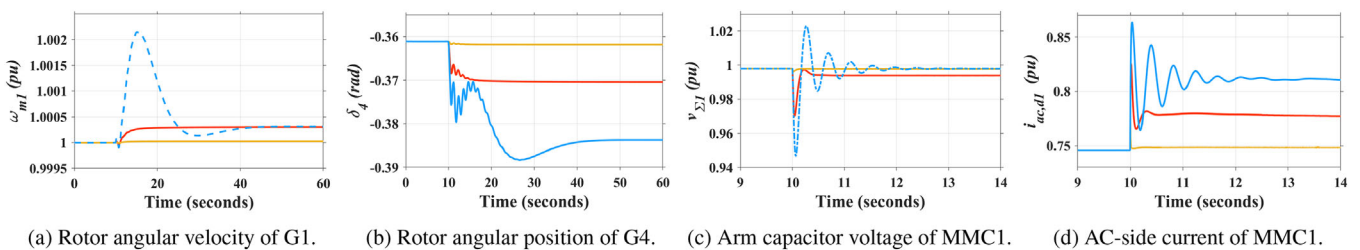

(a) Rotor angular velocity of G1.   (b) Rotor angular position of G4.   (c) Arm capacitor voltage of MMC1.   (d) AC-side current of MMC1.

FIGURE 11   Decentralized optimal controller performance after applying a 20% step increase to MMC1 reference AC-side active power at $t = 10$ s: (yellow) with decentralized optimal controller only, (blue) with MMC1 droop only, (red) with both decentralized optimal controller and MMC1 droop
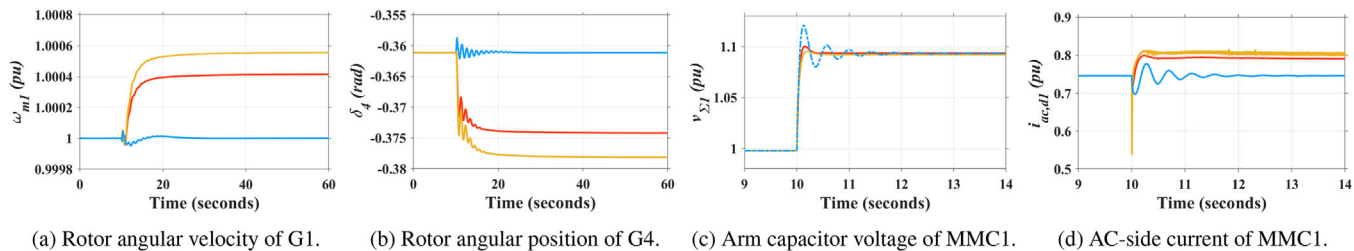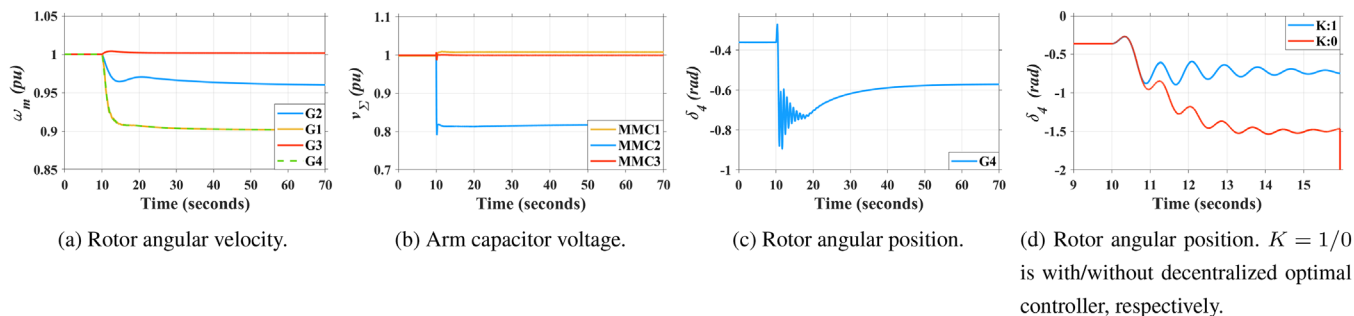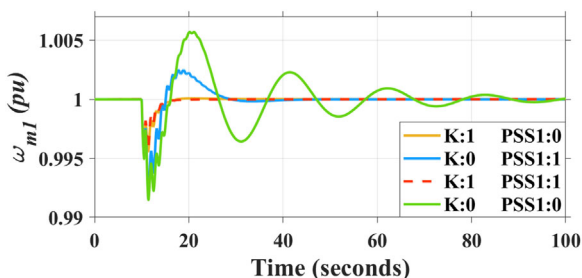
(a) Rotor angular velocity of G1. (b) Rotor angular position of G4. (c) Arm capacitor voltage of MMC1. (d) AC-side current of MMC1.

FIGURE 12 Decentralized optimal controller performance after applying a 20% step increase to MMC1 reference zero-sequence energy sum at $t = 10$ s: (yellow) with decentralized optimal controller only, (blue) with MMC1 droop only, (red) with both decentralized optimal controller and MMC1 droop

(a) Rotor angular velocity. (b) Arm capacitor voltage. (c) Rotor angular position. (d) Rotor angular position. $K = 1/0$ is with/without decentralized optimal controller, respectively.

FIGURE 13 Decentralized optimal controller performance under the worst-case perturbation scenario, $x_{0,worst}$, applied at $t = 10$ s

(a) Rotor angular velocity of G1.
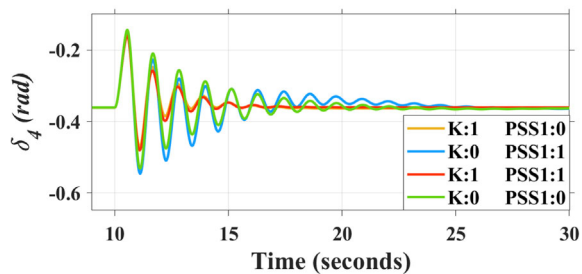
(b) Rotor angular position of G4.

FIGURE 14 Decentralized optimal controller performance under the three-phase short circuit fault at bus B2 applied at $t = 10$ s and cleared after 500 ms: (yellow) with decentralized optimal controller only, (blue) with PSS1 only, (red) with both decentralized optimal controller and PSS1, and (green) without both decentralized optimal controller and PSS1

ω_{m1} fluctuations after the fault and improve the grid stability compared with the PSS1.

Since the three-phase short circuit fault is the worst type of fault from the stability point of view [34], it can be concluded
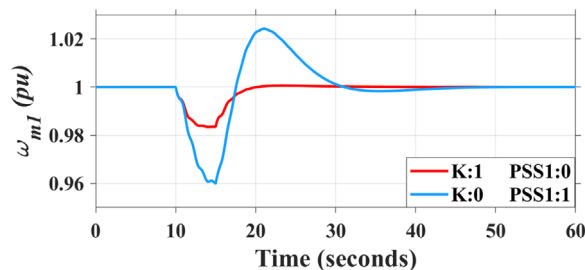

FIGURE 15 Performance comparison of the decentralized optimal controller and PSS1 under the three-phase short circuit fault at bus B2 applied at $t = 10$ s and cleared after 5 s
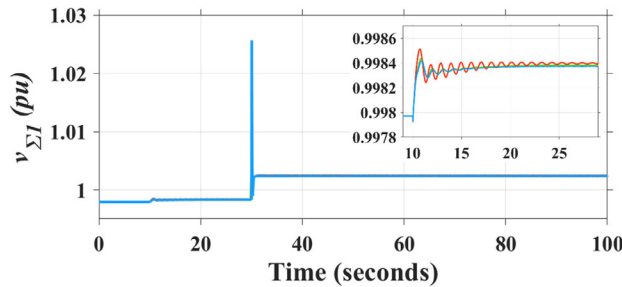
that the decentralized optimal controller can also be reliable to assure stability under other types of faults with the same clearing time as the three-phase fault. Additionally, the optimal controller presents better performance than the conventional PSS in minimizing the oscillations under the three-phase short circuit fault condition.

5.4 | Case Study IV: Robustness against parameter and operating point uncertainties

In this section, the decentralized optimal controller robustness in rejecting the impact of the parameter and operating point uncertainties is analysed. These uncertainties can arise from degradation, different operating and loading conditions, measurement errors, saturation, temperature variations, topology changes, and unmodelled fast dynamics of the switching devices [35]. Since the optimal controller is designed based on the
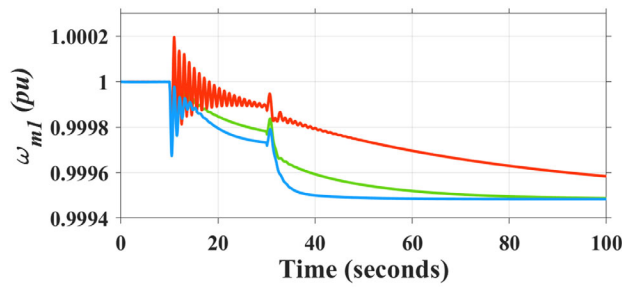
(a) Rotor angular velocity of G1.

(b) Arm capacitor voltage of MMC1.

FIGURE 16   Decentralized optimal controller dynamic performance with PSS1 gain of: (green) G_1, (blue) $G_1/5$, and (red) G_1*5
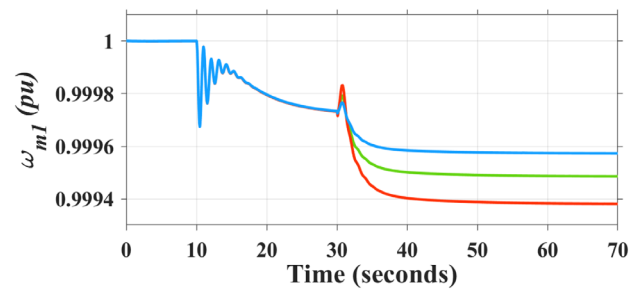

(a) Rotor angular velocity of G1.

(b) Arm capacitor voltage of MMC1.

FIGURE 17   Decentralized optimal controller dynamic performance with MMC1 droop gain of: (green) D_1, (blue) $D_1/2$, and (red) D_1*2

overall state-space model of the grid and linearized around a particular operating condition, its capability in handling uncertainties should be investigated. Hence, the dynamic performance of the optimal controller is evaluated when it is subject to uncertainties in control parameters, grid parameters, and operating conditions under a 2% step increase to G1 reference rotor angular velocity at $t = 10$ s (disturbance on the generator-side), and a 20% step increase to MMC1 reference AC-side active power at $t = 30$ s (disturbance on the converter side).

It is worth mentioning that the uncertainties considered in the grid parameters are fictitious and unrealistic since it is almost impossible to reach this level of parametric uncertainties in reality. However, the goal is to depict the robustness of the decentralized optimal controller to assure the grid's stability under the disturbances in the presence of parametric uncertainties.
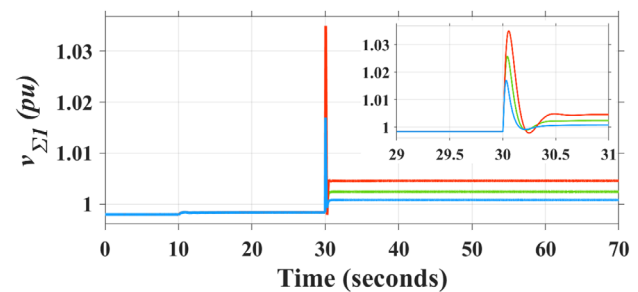
5.4.1 | Robustness against control parameter uncertainties

Control parameters may be poorly tuned without considering the interactions among grid equipment or need to be retuned due to grid reconfiguration. The two control parameters, which have the highest impact on the grid's stability, are the gains of the generator PSS1 and MMC1 droop controller.

Simulation results in Figures 16 and 17 show the optimal controller dynamic performance when it is subject to control parameters other than the ones it is tuned accordingly. In Figure 16, the PSS1 gain (-1) is divided and multiplied by five, resulting in gains of -0.2 and -5, respectively. As expected, the PSS1 gain variations affect the G1 rotor angular velocity more

than the MMC1 arm capacitor voltage. Moreover, the PSS1 gain increase makes the grid more prone to instability, as previously shown in Figure 7. On the other hand, Figure 17 depicts the simulation results for MMC1 droop gain (0.1) variation by halving (0.05) and doubling (0.2) its value, which is a conventional and reasonable range for droop gain variation. The effect of the various MMC1 droop gains become apparent after the disturbance on the MMC1 reference AC-side active power at $t = 30$ s is applied. The increase in the MMC1 droop gain causes the waveforms to have higher overshoot at the moment of the disturbance on the MMC side.

As is apparent from the figures, the decentralized optimal controller is robust enough to successfully perform and keep the grid stable under the disturbances when there are uncertainties in the most critical control parameters.

5.4.2 | Robustness against grid parameter uncertainties

Grid parameters may be wrongly measured/estimated or may vary due to degradation or equipment replacement. Hence, the robustness of the decentralized optimal controller is tested in this section against the uncertainties in the grid parameters, including the HVDC cable capacitance, MMC arm inductance, and generator synchronous reactance. Simulation results presented in Figures 18, 19, and 20 demonstrate the dynamic performance of the optimal controller when parameter uncertainties occur on the AC- and DC side of the grid.

As shown in Figure 18, increase/decrease of the MMC1 DC-side capacitance by multiplying/dividing it by five has a
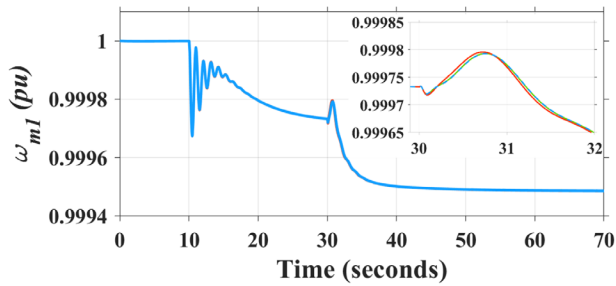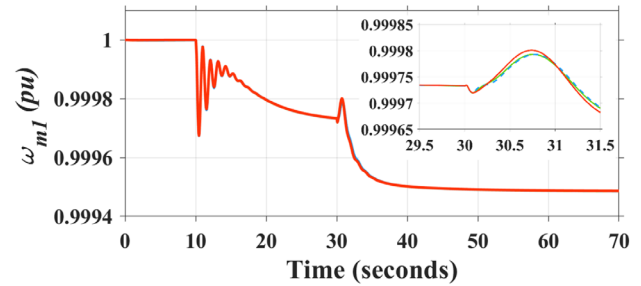
(a) Rotor angular velocity of G1.
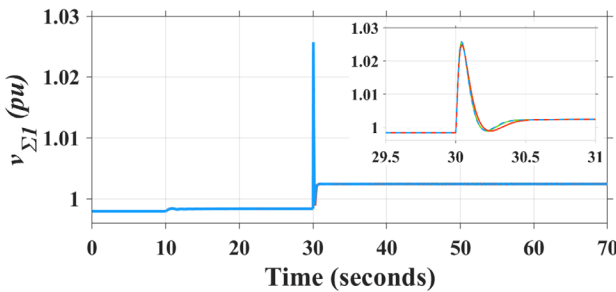
(b) Arm capacitor voltage of MMC1.

FIGURE 18 Decentralized optimal controller dynamic performance with MMC1 DC-side capacitance: (green) $(C_{dc1} + C_{dc1}/2)$, (blue) $(C_{dc1} + C_{dc1}/2)/5$, and (red) $(C_{dc1} + C_{dc1}/2)*5$
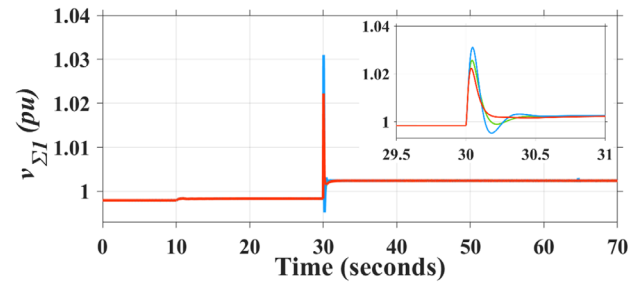

(a) Rotor angular velocity of G1.

(b) Arm capacitor voltage of MMC1.

FIGURE 19 Decentralized optimal controller performance with MMC1 arm inductance of: (green) L_{a1}, (blue) $L_{a1}/5$, and (red) $L_{a1}*5$

negligible effect on ω_{m1} and $v_{\Sigma1}$ waveforms. In other words, the uncertainty in the HVDC cable capacitance cannot cause instability under the decentralized optimal controller performance. On the other hand, Figures 19 and 20 depict the variation effect of the MMC1 arm inductance, L_{a1}, and G1 synchronous reactance, X_{d1}, on the decentralized optimal controller performance, respectively. As expected, the effect of the L_{a1} variation is more evident when the disturbance occurs on the converter side of the grid, whereas the disturbance on the generator side is more affected by the X_{d1} variation. In both cases, the optimal controller can keep the system stable under dynamics and transients.

5.4.3 | Robustness against grid operating conditions

Operating conditions can vary due to many reasons, including changes in grid source and load conditions. Since the decentralized optimal controller is designed under the operating condition depicted in Figure 1, its robustness against operating point uncertainty is tested by 30% increase and decrease of the AC load active power at bus B2, L_{B2}. The G1 active and reactive power by the increase of the L_{B2} become $P_{G1} = 909.4$ MW (44% increase) and $Q_{G1} = 57.4$ MVar while by the decrease of the L_{B2} become $P_{G1} = 338.5$ MW (46% decrease) and $Q_{G1} = -73.1$ MVar, respectively. Simulation results are shown in Figure 21. After exciting the electromechanical modes, $\lambda_{1,2}$, at $t = 10$ s, the rotor angular velocity of G1 varies by a max-

imum of about 2%. However, the decentralized optimal controller shows that it can handle the uncertainties of the operating condition and assure the grid's stability.

6 | DISCUSSION

6.1 | Pros and cons of the proposed methodology

The possibility of assuring the stability of the interconnected and expanded MMC-based hybrid AC/DC grid without running multiple time-consuming dynamic simulations and repetitive controllers' tuning of the grid equipment is probably the most prominent characteristic of the proposed decentralized optimal controller. This is because the controller is optimally designed under the grid worst-case perturbation/oscillation scenario and shows appropriate and satisfactory performance during the normal operating conditions as well as small and large disturbances. Furthermore, once the controller is designed using the grid state-space model, its operation is only dependent on local communication at every converter station, owing to the controller's decentralized configuration.

As mentioned earlier, the decentralized optimal controller's operation depends on the availability of all the grid dynamic state variables. These state variables can be measured or estimated through the WAMS, which can impose challenges due to the interoperability and presence of various operators and suppliers. Hence, measures are needed to run the controller successfully.
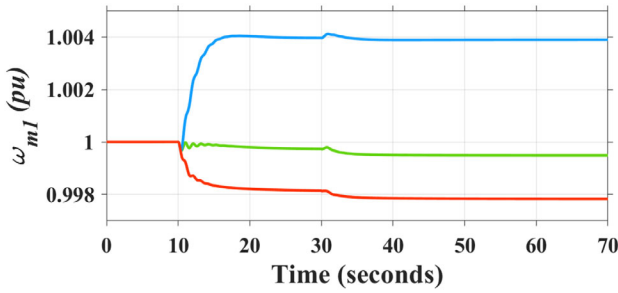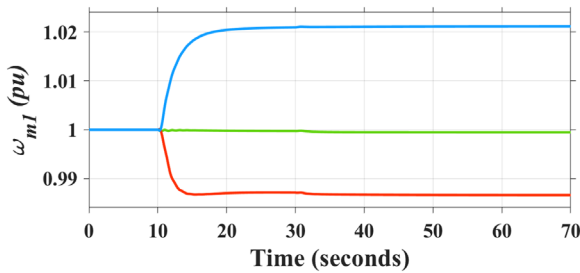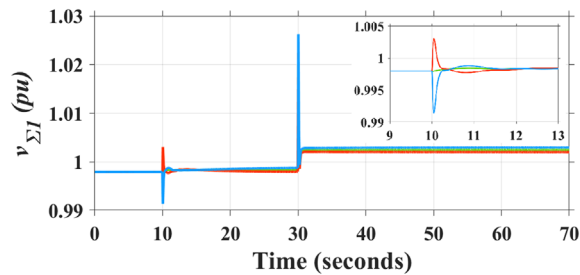
(a) Rotor angular velocity of G1.
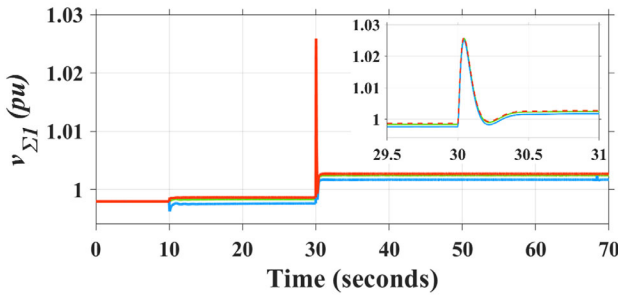
(b) Arm capacitor voltage of MMC1.

FIGURE 20 Decentralized optimal controller performance with G1 synchronous reactance of: (green) X_{d1}, (blue) $X_{d1}/2$, and (red) $X_{d1}*2$

(a) Rotor angular velocity of G1.

(b) Arm capacitor voltage of MMC1.

FIGURE 21 Decentralized optimal controller performance with load at bus B2 of: (green) L_{B2}, (blue) $L_{B2}*0.7$, and (red) $L_{B2}*1.3$

6.2 | Scalability of the proposed methodology

The scalability of the proposed methodology can be evaluated considering the communication and computational requirements as well as the optimization methodology.

The performance of the decentralized optimal controller, which can improve the grid's stability under the small and large dynamics and transients, is dependent on the zonal communication and computation of the grid's state variables, as can be seen in Figure 3. Evidently, if the communication between the grid equipment and controller is lost in one zone, the decentralized optimal controller cannot function as intended in that zone. However, if the decentralized optimal controller is operating as an additional controller in the presence of the PSS and MMC droop controller, the loss of communication does not affect the conventional performance of the grid. The decentralized optimal controller can function properly again if the communication is restored. It is worth mentioning that since the optimal controller is decentralized (block-diagonal), an increase in the grid size does not affect the controller's performance.

On the other hand, the scalability of the proposed optimization problem is mostly dependent on the applied methodology. As mentioned earlier, the optimization formulation is approximated as a convex SDP problem using the Lyapunov stability and LMI theories. Hence, as long as the optimization methodology's inputs ($A_{n\times n}$, $B_{n\times m}$, and $C_{n\times n}$) are available, and the optimization matrices (E_x^i, E_u^j, and Y) are reasonably tuned/selected, it should scale adequately with the grid size increase thanks to convexity and linearity. However, it should be noted that obtaining the optimization methodology's inputs, which are the grid state-space matrices, could be challenging when the number of the grid state variables increases and the system becomes large and highly complex. Moreover, if the optimization matrices are not tuned appropriately and reasonably, there might be convergence issues under some control inputs and state variables. Therefore, to improve the methodology's scalability in large-scale hybrid AC/DC grids, it might be necessary to further reduce the modelling order of the grid equipment.

7 | CONCLUSION

This paper investigated the applicability of a decentralized optimal linear feedback controller in improving the stability margins and minimizing the oscillations caused by the poorly damped modes in an MMC-based multiterminal hybrid AC/DC grid. The optimal controller, which can be derived analytically, can assure the stability of the interconnected grid without the need for running time-consuming dynamic simulations and repetitive controllers' tuning. Furthermore, the controller's decentralized architecture can help avoid long-distance communication delays and failures threatening the network's reliability and stability.

Two pairs of poorly damped modes were found via the small-signal eigenvalue stability analysis ($\lambda_{1,2}$ and $\lambda_{3,4}$). One pair, $\lambda_{1,2}$, was an inter-area electromechanical mode associated with the generator's rotor angular velocity and position, whereas the other pair, $\lambda_{3,4}$, was linked with the MMC arm capacitor voltages. It was shown that the decentralized optimal controller can improve the damping ratio of the former pair (mode on the generator-side) by 2.34 times and the latter one (mode on the

converter-side) by 4.05 times, and enhance the stability margins of the grid by pushing these modes further away from the right half-plane ($\lambda_{1,2}$: from -0.27 to -0.67, and $\lambda_{3,4}$: from -2.13 to -10.54). Such phenomena would have been ignored if detailed models on both sides of the grid were not being applied.

Time-domain simulations revealed interactions and propagation of the oscillations and disturbances between the generator side (AC side) and converter side (DC side) of the grid. The state variables involved, which are the rotor angular velocity and position on the AC side and MMC arm capacitor voltage on the DC side, also contribute to the poorly damped modes of the grid and are very sensitive to the PSS and MMC droop controller tuning parameters/gains. The higher these gains, the lower the grid stability margins, making the grid more prone to instability.

It was proved that the decentralized optimal controller can efficiently operate in the absence or presence of the PSS or droop controller to reduce the oscillations that occur due to the poorly damped modes' excitation and keep the system stable. In some cases, the optimal controller can take advantage of the energy stored in the MMC arm capacitors by manipulating the arm capacitor voltages to minimize the oscillations originating from the AC side of the grid. It was also demonstrated that the optimal controller can ensure system stability under small and large disturbances and has better performance to limit the rotor angular velocity and position variations than the PSS under the three-phase short-circuit fault condition. Since this type of fault is the worst type from the stability point of view, it can be concluded that the decentralized optimal controller can also be reliable to guarantee stability under other types of faults.

Last but not least, the robustness of the decentralized optimal controller is evaluated against the uncertainties in control parameters, grid parameters, and operating conditions under the disturbances on the AC- and DC side of the grid. The control parameters' uncertainties were modeled by varying the PSS gain and MMC droop gain. The grid parameters of interest were the generator synchronous reactance, MMC arm inductance, and DC-side capacitance. Additionally, an AC load was changed by $\pm 30\%$ to simulate the uncertainties in operating conditions. It is shown that the decentralized optimal controller is robust enough to keep the grid stable under disturbances when it is subject to all the abovementioned uncertainties.

As a potential future work, the feasibility and practicality of the proposed methodology can be investigated through an experimental test. Namely, the performance of the decentralized optimal controller can be analysed using one (or more) physical MMC in power hardware in the loop (PHIL) setting to simulate the realistic grid conditions.

CONFLICT OF INTEREST
The authors have declared no conflict of interest.

DATA AVAILABILITY STATEMENT
The data that support the findings of this study are available from the corresponding author upon reasonable request.

ORCID
Atousa Elahidoost https://orcid.org/0000-0003-3433-9398
Elisabetta Tedeschi https://orcid.org/0000-0002-6185-4910

REFERENCES
1. Zappa, W., Junginger, M., van den Broek, M.: Is a 100% renewable european power system feasible by 2050? Appl. Energy 233-234, 1027–1050 (2019). Available from: https://www.sciencedirect.com/science/article/pii/S0306261918312790.
2. Ansari, J.A., Liu, C., Khan, S.A.: MMC based MTDC grids: a detailed review on issues and challenges for operation, control and protection schemes. IEEE Access 8, 168154–168165 (2020)
3. Wang, M., An, T., Ergun, H., Lan, Y., Andersen, B., Szechtman, M., Leterme, W., Beerten, J., Van Hertem, D.: Review and outlook of HVDC grids as backbone of the transmission system. CSEE J. Power Energy Syst. 7(4), 797–810 (2021)
4. Elahidoost, A., Tedeschi, E.: Expansion of offshore HVDC grids: an overview of contributions, status, challenges and perspectives. In: 2017 IEEE 58th International Scientific Conference on Power and Electrical Engineering of Riga Technical University (RTUCON), pp. 1–7 (2017)
5. Shah, R., Sánchez, J.C., Preece, R., Barnes, M.: Stability and control of mixed AC-DC systems with VSC-HVDC: a review. IET Gener. Transm. Distrib. 12, 2207–2219(12) (2018)
6. Bayo Salas, A.: Control Interactions in power systems with multiple VSC HVDC converters. Ph.D. thesis. KU Leuven, Leuven, Belgium (2018)
7. Pinares, G., Bongiorno, M.: Analysis and mitigation of instabilities originated from dc-side resonances in VSC-HVDC systems. IEEE Trans. Ind. Appl. 52(4), 2807–2815 (2016)
8. Taffese, A.A., Endegnanew, A.G., D'Arco, S., Tedeschi, E.: Power oscillation damping with virtual capacitance support from modular multilevel converters. IET Renewable Power Gener. 14(5), 897–905 (2020)
9. Buchhagen, C., Rauscher, C., Menze, A., Jung, J.: Borwin1—first experiences with harmonic interactions in converter dominated grids. In: International ETG Congress 2015; Die Energiewende - Blueprints for the new energy age, pp. 1–7 (2015)
10. Saad, H., Fillion, Y., Deschanvres, S., Vernay, Y., Dennetière, S.: On resonances and harmonics in HVDC-MMC station connected to ac grid. IEEE Trans. Power Delivery 32(3), 1565–1573 (2017)
11. Zhou, Q., Ding, Y., Mai, K., Bian, X., Zhou, B.: Mitigation of subsynchronous oscillation in a VSC-HVDC connected offshore wind farm integrated to grid. Int. J. Electr. Power Energy Syst. 109, 29–37 (2019). Available from: https://www.sciencedirect.com/science/article/pii/S0142061518326711
12. Yin, C., Xie, X., Xu, S., Zou, C.: Review of oscillations in vsc-hvdc systems caused by control interactions. J. Eng. 2019(16), 1204-1207 (March 2019)
13. Agbemuko, A.J., Domínguez García, J.L., Gomis Bellmunt, O.: Impedance-based modelling of hybrid ac/dc grids with synchronous generator for interaction study and dynamic improvement. Electr. Power Syst. Res. 179, 106086 (2020). Available from: https://www.sciencedirect.com/science/article/pii/S0378779619304055
14. Gonzalez Torres, J.C., Damm, G., Costan, V., Benchaib, A., Lamnabhi Lagarrigue, F.: Transient stability of power systems with embedded VSC-HVDC links: stability margins analysis and control. IET Gener. Transm. Distrib. 14, 3377–3388(11) (2020)
15. Dewangan, L., Bahirat, H.J.: Controller interaction and stability margins in mixed SCR MMC-based HVDC grid. IEEE Trans. Power Syst. 35(4), 2835–2846 (2020)

16. Fuchs, A., Imhof, M., Demiray, T., Morari, M.: Stabilization of large power systems using VSC-HVDC and model predictive control. IEEE Trans. Power Delivery 29(1), 480–488 (2014)

17. Gonzalez Torres, J.C., Damm, G., Costan, V., Benchaib, A., Lamnabhi Lagarrigue, F.: A novel distributed supplementary control of multi-terminal VSC-HVDC grids for rotor angle stability enhancement of ac/dc systems. IEEE Trans. Power Syst. 36(1), 623–634 (2021)

18. Guo, C., Yang, S., Liu, W., Zhao, C.: Single-input-single-output feed-back control model and stability margin analysis for hybrid dual-infeed HVDC system. IEEE J. Emerg. Sel. Top. Power Electron. 9(3), 3061–3071 (2021)

19. Zou, Y., Qin, J., Zhang, L., Yu, J.: Inequality constraints based method for fast estimation of droop slope stability regions for MMC-based MTDC systems. IEEE Trans. Power Delivery 36(6), 3689–3700 (2021)

20. Guo, C., Cui, P., Zhao, C.: Optimization and configuration of control parameters to enhance small-signal stability of hybrid LCC-MMC HVDC system. J. Mod. Power Syst. Clean Energy 10(1), 213–221 (2022)

21. Lyu, J., Cai, X., Molinas, M.: Optimal design of controller parameters for improving the stability of MMC-HVDC for wind farm integration. IEEE J. Emerg. Sel. Top. Power Electron. 6(1), 40–53 (2018)

22. Huang, T., Yang, F., Zhang, D., Chen, X.: High-frequency stability analysis and impedance optimization for an MMC-HVDC integrated system considering delay effects. IEEE J. Emerging Sel. Top. Circuits Syst. 12(1), 59–72 (2022)

23. Elahidoost, A., Furieri, L., Kamgarpour, M., Tedeschi, E.: Optimal linear controller for minimizing dc voltage oscillations in MMC-based offshore multiterminal hvdc grids. IEEE Access 9, 98731–98745 (2021)

24. Fuchs, A., Morari, M.: Actuator performance evaluation using LMIs for optimal HVDC placement. In: 2013 European Control Conference (ECC), Zurich, Switzerland, pp. 1529–1534 (2013) https://doi.org/10.23919/ECC.2013.6669747

25. Kundur, P.: Power System Stability and Control. McGraw-Hill, New York, NY (1994)

26. Leterme, W., Ahmed, N., Beerten, J., Ängquist, L., Hertem, D.V., Norrga, S.: A new HVDC grid test system for HVDC grid dynamics and protection studies in EMT-type software. In: 11th IET International Conference on AC and DC Power Transmission, Birmingham, pp. 1–7 (2015) https://doi.org/10.1049/cp.2015.0068

27. Bergna-Diaz, G., Suul, J.A., D'Arco, S.: Energy-based state-space representation of modular multilevel converters with a constant equilibrium point in steady-state operation. IEEE Trans. Power Electron. 33(6), 4832–4851 (2018)

28. Sanchez, S., Bergna, G., Tedeschi, E.: Tuning of control loops for grid-connected modular multilevel converters under a simplified port representation for large system studies. 2017 Twelfth International Conference on Ecological Vehicles and Renewable Energies (EVER), Monte Carlo, Monaco, pp. 1–8 (2017) https://doi.org/10.1109/EVER.2017.7935913

29. Beerten, J., D'Arco, S., Suul, J.A.: Frequency-dependent cable modelling for small-signal stability analysis of VSC-HVDC systems. IET Gener. Transm. Distrib. 10(6), 1370–1381 (2016)

30. Fuchs, A., Morari, M.: Placement of HVDC links for power grid stabilization during transients. In: 2013 IEEE Grenoble Conference, Grenoble, France, pp. 1–6 (2013) https://doi.org/10.1109/PTC.2013.6652508

31. Elahidoost, A., Tedeschi, E.: Control optimization of the offshore hvdc grid based on modular multilevel converter for improving dc voltage stability. Renew. Energy Power Qual. J. 18, 207–212 (2020)

32. Lofberg, J.: YALMIP: a toolbox for modeling and optimization in MAT-LAB. In: 2004 IEEE International Conference on Robotics and Automation (IEEE Cat. No.04CH37508), Taipei, Taiwan, pp. 284–289 (2004) https://doi.org/10.1109/CACSD.2004.1393890

33. Andersen, E.D., Andersen, K.D.: The mosek interior point optimizer for linear programming: an implementation of the homogeneous algorithm. In: Frenk, H., Roos, K., Terlaky, T., Zhang, S., editors. High Performance Optimization, pp. 197–232. Springer US, Boston, MA (2000). Available from: https://doi.org/10.1007/978-1-4757-3216-0_8

34. Das, J.C.: Short-Circuits in AC and DC Systems: ANSI, IEEE, and IEC Standards. CRC Press, Taylor & Francis Group, USA (2017)

35. Belhaouane, M.M., Ayari, M., Guillaud, X., Braiek, N.B.: Robust control design of MMC-HVDC systems using multivariable optimal guaranteed cost approach. IEEE Trans. Ind. Appl. 55(3), 2952–2963 (2019)